

Non-standard risk monitoring

Deliverable D3.4: An ad-hoc risk monitoring strategy report including specific recommendations for industrial geothermal projects and insurance companies

Lead Beneficiary	
Type	<input checked="" type="checkbox"/> R - report, document etc. <input type="checkbox"/> OTHER - software, technical diagram etc. <input type="checkbox"/> DEM - demonstrator, pilot etc. <input type="checkbox"/> E - ethics <input type="checkbox"/> DEC - website, patent filing etc.
Status	<input type="checkbox"/> Draft <input checked="" type="checkbox"/> WP manager accepted <input checked="" type="checkbox"/> Project coordinator accepted
Dissemination level	<input checked="" type="checkbox"/> PU - Public <input type="checkbox"/> CO - Confidential: only for members of the consortium
Contributors	<input checked="" type="checkbox"/> 1-GFZ <input type="checkbox"/> 5-GES <input type="checkbox"/> 9-GTL <input type="checkbox"/> 13-SNU <input type="checkbox"/> 2-ENB <input type="checkbox"/> 6-TNO <input checked="" type="checkbox"/> 10-UoS <input type="checkbox"/> 14-KIC <input checked="" type="checkbox"/> 3-ESG <input type="checkbox"/> 7-ETH <input type="checkbox"/> 11-TUD <input type="checkbox"/> 15-ECW <input type="checkbox"/> 4-UoG <input type="checkbox"/> 8-GTN <input type="checkbox"/> 12-NEX <input type="checkbox"/> 16-WES
Creation date	30.04.2019
Last change	26.08.2019
Version	Final
Due date	31.08.2019
Submission date	27.08.2019

Authors

Authors from UoS: Azzola, J.1, Schmittbuhl, J.1, Zigone, D.1, Lengliné, O.1, Magnenet, V.2, Masson, F.1 Institut de Physique du Globe de Strasbourg, Université de Strasbourg/EOST, CNRS, France
2 ICUBE, 72 Route du Rhin, Illkirch, France

Authors from GFZ Potsdam: Fleming, K., Pittore, M., Megalooikonomou, K. G.

Authors from ESG Strasbourg: Maurer, V., Richard, A., Genter, A.

Publication Date

August 2019

Table of content

1	Introduction	3
2	Non-standard risk monitoring around operational geothermal plants	3
3	Risk monitoring methodologies	7
4	Coda Wave Interferometry based monitoring techniques	12
4.1	Introduction	12
4.2	Analysis of the time-delays measured during the elastic deformation of the sample, at laboratory scales	14
4.3	Temporal and spatial variability of decoherence during the elastic deformation, at the laboratory scale	23
4.4	Upscaled numerical model	27
4.5	Conclusions and recommendations	32
5	Bibliography	34

1 Introduction

The following public report, “Non-standard risk monitoring”, corresponds to Deliverable 3.4 of the European DESTRESS project. This report was produced within the framework of Work Package (WP) 3 dealing with “Risk management workflows for deep geothermal energy” and involved scientific staff from GFZ (Potsdam), UoS (Strasbourg) and ESG (Strasbourg).

Enhanced geothermal systems (EGS) allow the widespread use of the enormous potential of untapped geothermal energy. EGS measures are generally intended to improve productivity (or injectivity) of a geothermal reservoir by increasing the overall transmissivity of the reservoir rocks. This goal is achieved by various methods that are dependent upon the geological system in question, comprising the rocks, the rock structures, the tectonic situation, as well as the stress field (Huenges et al., 2020).

Within the framework of DESTRESS, the objective behind risk management for deep geothermal energy deals with risk governance during soft stimulation operations, both chemical and hydraulic, of geothermal reservoirs, as well as for sustainable operations such as long-term exploitation (Baujard et al., 2017; Baujard et al., 2018). Thus, a series of risk assessment and workflows have been developed for both soft chemical stimulation (Peterschmitt et al., 2018) and for seismic risk related to hydraulic stimulation (Grigoli et al., 2017). Such methodologies aim to provide to operators a reliable decision tool to estimate environmental risks, such as induced seismicity following reservoir operations. Thus, an Adaptive Traffic Light System (ATLS) has been developed and tested with real and synthetic datasets (Grigoli et al., 2018; Mignan et al., 2019). This system takes into account, in a probabilistic way, data such as real time induced seismicity and geomechanical models.

In parallel to such risk assessment, several public acceptance studies have been run in various EU countries (France, Germany, UK) with various methodologies (Chavot et al., 2018). Most of them were done in areas where geothermal stimulations have been undertaken, namely France, Switzerland, the UK, and the Netherlands (Chavot et al., 2019; Ejderyan et al., 2019, Cees et al. 2020).

Finally, risk management was also studied by investigating the risk related to the stimulation or sustainable exploitation of geothermal resource by using non-standard monitoring techniques. Sensors have been deployed in the field in Northern Alsace for investigating buildings’ vulnerability to induced ground motion during the operation of two geothermal plants located in this area. A set of 500 buildings were surveyed in an area of around 130 km² (Megalooikonomou et al., 2018; Pittore et al., 2018). This comprised field work around the operational power plant of Soultz and the geothermal plant of Rittershoffen, as well as experimental work and numerical modelling activities on CWI (Coda Wave Interferometry), reproducing the mechanical and acoustic behaviour of typical reservoir rock (Azzola et al., 2018a, b). A specific analysis for characterizing the present-day stress field in the vicinity of the Rittershoffen geothermal wells has been done (Azzola et al., 2019).

The purpose of this deliverable 3.4 is to focus on non-standard risk monitoring.

2 Non-standard risk monitoring around operational geothermal plants

Non-standard risk monitoring study is an important challenge being examined within the framework of DESTRESS. A semi-analytical model for describing the seismic performance of the types of buildings defined in the derived exposure modelling has been developed following the methodology described in Megalooikonomou et al. (2018). In particular, the modelling focused on the computation of fragility curves describing the probability of exceeding a first level of non-structural damage

(Megalooikonomou et al., 2018). In order to calibrate the analytical model, a set of buildings was selected for field measurements in Alsace around the geothermal sites. The vulnerability modelling focused on buildings constructed of unreinforced masonry, which may be more susceptible to the range of ground motion expected in the event of induced seismicity in the area. The measurements have been carried out using the MPwise (Multi-Parameter Wireless Sensing System) smart device (Boxberger et al., 2017), which has been designed to carry out rapid measurement activities by exploiting the computing and advanced networking capacities embedded in individual units. Based on measurements of environmental seismic noise, the fundamental frequency of vibration of the inspected buildings has been estimated and used to calibrate the respective fragility curves.

In collaboration with GFZ, ES-Géothermie organized a three days acquisition campaign from the 16th to 18th October 2017 which involved the installation of four sets of sensors in private houses located in villages located around the Soultz and Rittershoffen geothermal sites. The fundamental period of these structures was verified by analysing the ambient noise measured using the MPwise sensors, with one sensor installed outside of the buildings, and the three others installed on each floor of the houses (basement, ground floor and first floor). The sensors were installed to record the ambient noise and to draw a vulnerability mode that allows the issuing of damage forecasts. As shown in Figure 1, in total, 11 houses were monitored, selected to provide a representative sample of the different types of masonry in this area of Alsace (timber frame, concrete frame, etc.).

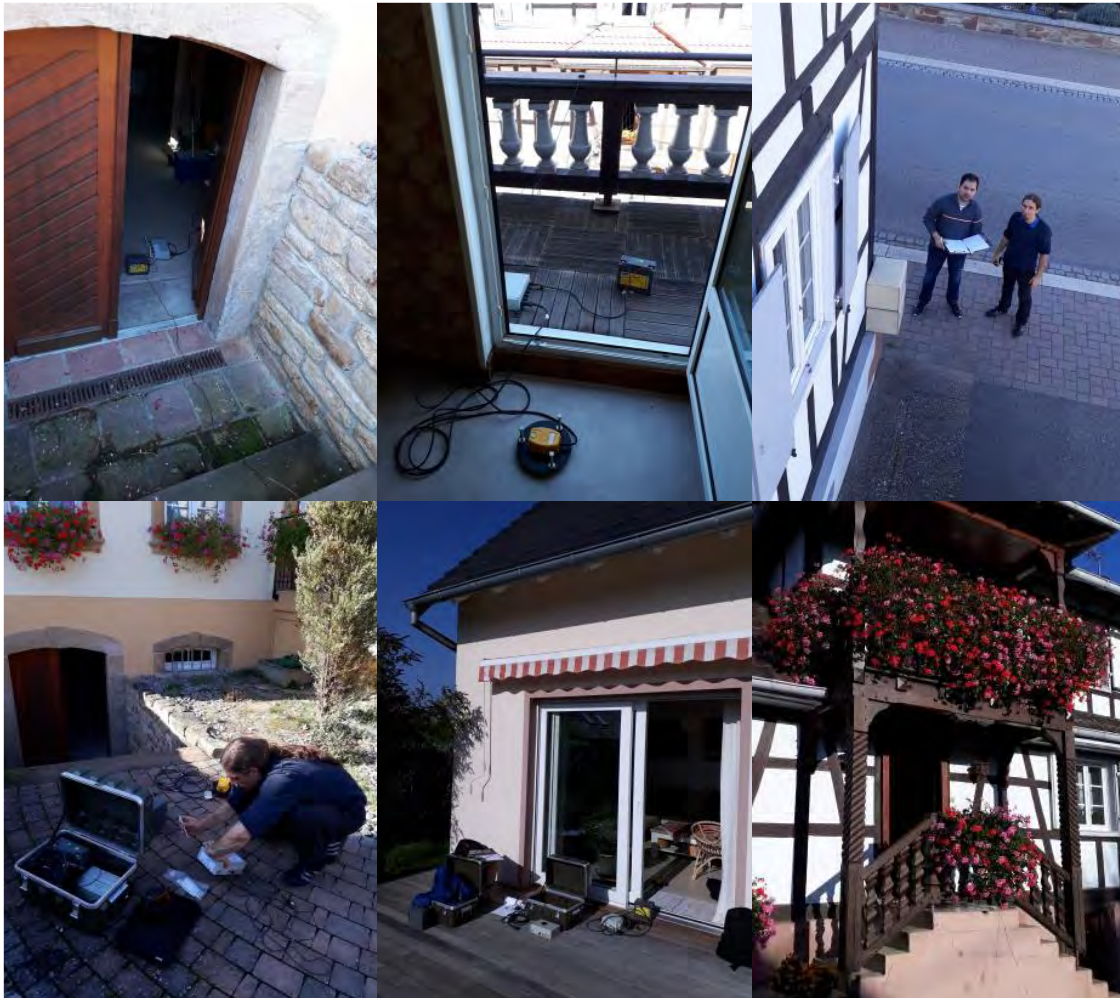


Figure 1 Series of pictures taken during the acquisition campaign. A set of 11 buildings was selected for field measurements in Alsace around the geothermal sites to measure the fundamental period of these structures by analysing the ambient noise measured using the MPwise sensors.

In order to acknowledge local population for their kindness in permitting the sensors' installation in their homes, a visit of the Rittershoffen geothermal plant was organized. After a short presentation of the project, the 15 people present had the chance to visit the different installations of the plant. Many questions were asked at this occasion, and people went back with a better idea of the advantages and the challenges of deep geothermal project.



Figure 2 Visit of the Rittershoffen geothermal plant to thank local people that accepted the installation of the sensors in their homes.

Then, a methodology for defining and assigning custom seismic vulnerability classes to residential buildings was developed and tested on a set of 500 buildings surveyed in an area of around 130 km² around the two geothermal plants pumping flowrate of 280m³/h and 100m³/h for Rittershoffen and Soultz respectively. The methodology allows a post-acquisition modelling of exposure based on faceted taxonomies and a fuzzy scoring system (Pittore et al., 2018) and is suitable for rapid, but efficient and traceable risk estimation applications. A total of 7 classes have been defined, which characterize the targeted built environment in terms of building practices and structural materials.

A prototype MPwise sensor was established on the 14th May 2018 in the town hall of the village of Keffenach, located several kilometres from Soultz-sous-Forêts, with the support of the local mayor office (see Figure 2). The sensor was customized by considering the specific fragility model of the building where the sensor is installed, knowing that the building had been previously screened. The sensor is collecting 3-axis strong-motion data and sending it in real time to GFZ and to the geothermal plant located in the vicinity of the building. In case of an induced event, the sensor is programmed to issue a local and remote warning in case the ground motion that could potentially lead to non-structural damage encoded in the fragility model is expected to be exceeded. Since the detection methodology is based on P-wave analysis, the warning can be issued before the arrival of the slower, but stronger S-waves, thus representing a prototype decentralized early warning system (Megalooikonomou et al., 2018).



Figure 3 A prototype MP-Wise sensor installed on May the 14th 2018 in the town hall of the village of Keffenach. The sensor was customized by considering the specific fragility model of the building.

In parallel to this non-standard risk monitoring system, some research was conducted on the application of CWI (Coda Wave Interferometry) to ambient seismic noise correlation, referred to as Ambient Noise Interferometry (ANI), which has found a large range of applications in recent years, such as for reservoir monitoring. As fluid injections can also trigger non-seismic (or aseismic) displacements, monitoring methods applied in reservoir management are generally based on micro seismicity. However, in order to constantly follow a reservoir's evolution (seismic and aseismic deformations), including fine-scale methods, it is important to develop tools that can be applied independently of the spatio-temporally-dependent seismicity. Physically, the changes in phases observed are typically interpreted as small variations in seismic velocities. However, this interpretation remains questionable. The research activities on the influence of the elastic deformation of the medium on coda wave interferometry measurements, which could support a new interpretation of coda wave interferometry, have focused on several aspects of direct numerical modelling, a comparison between experimental and numerical modelling approaches during mechanical deformation, and the development of a 2D numerical analysis replicating experiments conducted on granite samples (Azzola et al., 2018a, b).

3 Risk monitoring methodologies

During the DESTRESS project, GFZ was concerned with developing monitoring and modelling procedures for the risk associated with induced seismicity resulting from geothermal exploitation activities. The main concern, considering the relatively small ground motion usually associated with induced seismicity, has to do with non-structural seismic damage, which nonetheless has the potential

to see noticeable economic losses and the disruption of activities associated with infrastructure such as hospitals. The relevant activities undertaken by GFZ may be divided, in general, into two parts:

- The monitoring of seismic risk and development of fragility curves (Megalooikonomou et al., 2018).
- Development of taxonomies for modelling building portfolios (Pittore et al., 2018).

The developed methodologies were tested by considering one of the DESTRESS test sites, namely the village of Soultz-sous-Forêts in Alsace, France. The area has a very low level of natural seismicity, but it has experienced induced seismicity as a result of the geothermal plant activity either during previous stimulation operations or during geothermal exploitation (Dorbath et al., 2009; Cuenot et Genter, 2015; Baujard et al., 2018).

In the framework of DESTRESS, the village and surrounding area were surveyed using the remote rapid visual screening (RRVS) methodology (Figure 1), which consists of an omni-directional camera system installed on a vehicle which is driven around the area of interest. The resulting images are then imported into a web-based platform which includes a GIS map interface, from which an engineer assigns a series of attributes to each considered building (Haas et al., 2016).

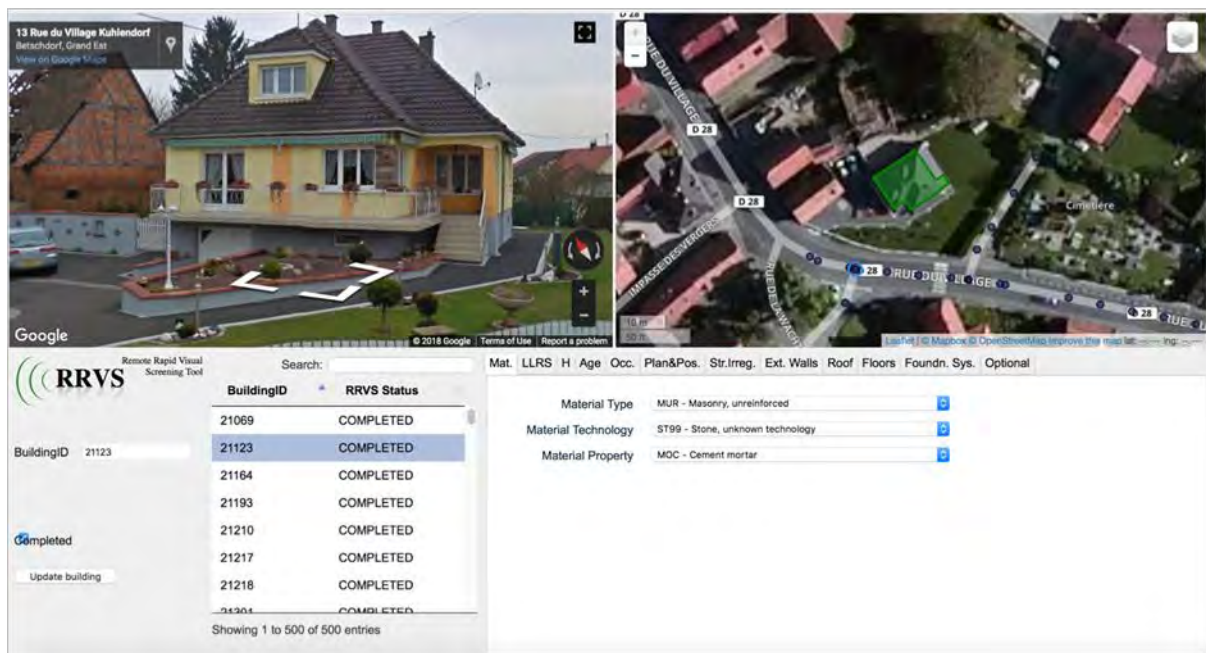


Figure 4 Graphical User Interface (GUI) of the RRVS web-based platform. The bottom side includes multiple tabs for the manual entry of the observed structural features. The upper left panel shows an example of an omnidirectional image of a building located in the Soultz-sous-Forêts village, while in the upper right panel the same building (in green the related footprint) is shown in a GIS map (Pittore et al., 2018).

When considering the monitoring of risk, or as is described by the work undertaken, the development of a performance-driven system, the first requirement is an exposure model, which describes the elements that are exposed to a specific hazard (i.e., what is found from carrying out the RRVS). As mentioned, an engineer, making use of the acquired images and GIS database, assigns attributes to the buildings in question, both structural and non-structural. The taxonomy used in these activities is that developed within the Global Earthquake Model (GEM) initiative ¹. This taxonomy employs 13

¹ [HTTPS://STORAGE.GLOBALQUAKEMODEL.ORG/WHAT/PHYSICAL-INTEGRATED-RISK/BUILDING-TAXONOMY/](https://storage.globalquakemodel.org/what/physical-integrated-risk/building-taxonomy/)

building attributes that allow an overview of the types of buildings that are in the area under investigation and which are exposed to seismic hazard. The GEM taxonomy is described as a faceted taxonomy, as it is a more bottom-up approach, where by taxonomies such as that provided by HAZUS, termed risk-orientated taxonomies, classify structures as a whole. Making use of the GEM taxonomy, we have classified around 500 buildings in the Soultz-sous-Forêts area (Figure 2).

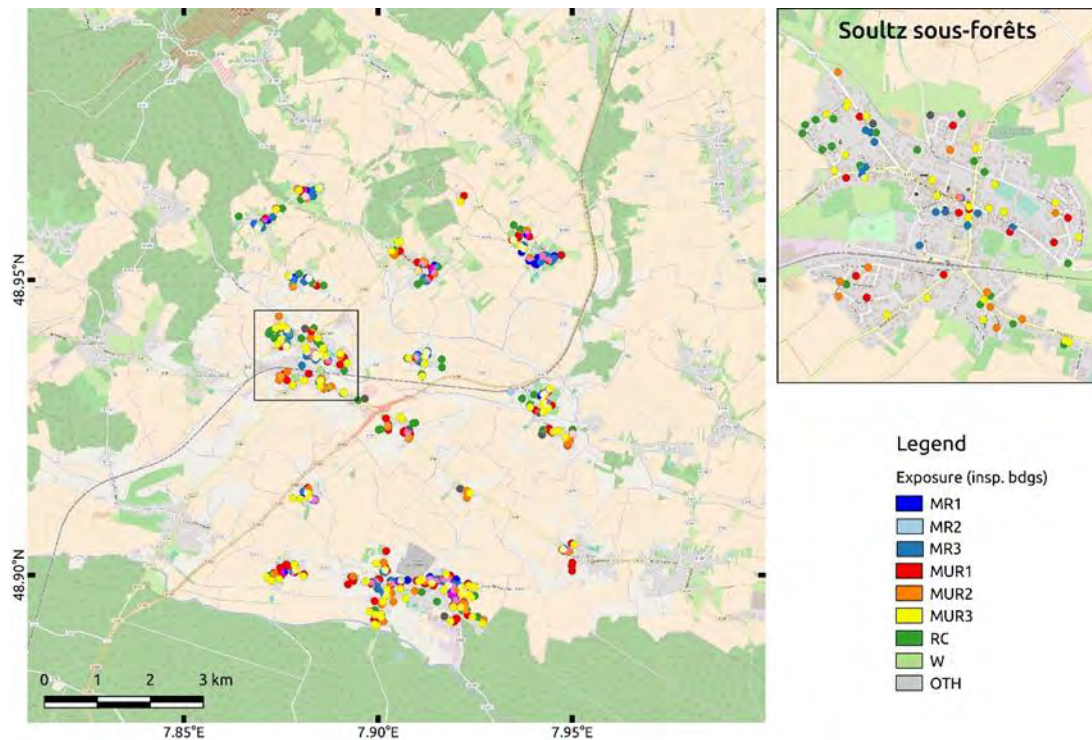


Figure 5 The exposure model developed for the town and district of Soultz-sous-Forêts (from Megalooikonomou et al., 2018). The various classifications are as follows: MUR = Unreinforced Masonry, MR = Reinforced Masonry, RC = Reinforced Concrete, W = Wood, OTH = Other, 1= One floor - building, 2 = Two floors - building with rigid diaphragm, 3 = Two floors -building with flexible diaphragm.

What is now required is the development of appropriate fragility curves in order to describe the relationship of the building's response to a given level of ground motion. This requires an engineering demand parameter (EDP), which in the case of the non-structural elements being investigated, involves the maximum interstory drift ratio (IDR) or the peak floor acceleration (PFA). Once such curves are developed, they may be incorporated into rapid damage forecasting systems. This calls upon the monitoring of real-time strong motion, where the initial P-wave arrivals are analysed by determining various parameters from the preliminary ground motion that allow an estimation of the intensity of the forthcoming S- and surface waves. A decision may then be made with regards to whether or not to issue an alert, or to provide an estimate of what the expected damage will be for a given structure based on their fragility curve. One means of determining such curves is by the use of the equivalent degree-of-freedom system (ESDOF).

As part of activities undertaken for DESTRESS, Megalooikonomou et al. (2018) considered in some details, two general classes of structures: unreinforced masonry (URM) and timber framed masonry (TFM). These types of structures occur in relatedly high numbers in the mostly rural areas that surround the geothermal platform considered in these activities. For the URM, the authors made use of a modified version of the ESDOF method, as proposed by Vamvatsikos and Pantazopoulou (2015), considering only key-geometric characteristics describing a box-shaped masonry building, along with factors such as wall thickness, shear strength and shear modulus. The method involves defining the

fundamental vibration mode by approximating it by a 3D shape function which is consistent with the building's boundary conditions. This brings up a limiting factor behind the use of this method, as it is not applicable to irregularly shaped buildings. For TFM, a similar approach is employed to derive the ESDOF properties, making use of only the key geometric characteristics of the timber panels and their strength, without considering the infill masonry walls.

Use was made of realistic induced ground motion records. These were found from the web-based Pacific Earthquake Engineering Research Centre (PEER) ground motion database . A selection of records was made, covering moment magnitudes between 3 and 5.5, depths from 3 to 14 km, with epicentral distances between 5 and 55 km. For the URM buildings, these records were used as input to an analysis that made use of results from shake-table experiments (Bothara et al., 2010) leading to fragility curves for the pre-yielding damage state. The curves employed the incremental dynamic analysis of the ESDOF derived from the table experiments. For the TFM, given that there are no shake table experiments for such structures, the fragility curves were defined through the non-linear static analysis of TFM walls, using a model adapted from Kouris and Kappos (2014), again employing the PEER recordings for the IDA.

Figure 3 shows the resulting fragility curves for the case of such buildings in the study area. These were derived in terms of Peak Ground Acceleration (PGA) making use of the MATLAB toolbox FEDEAS (Filippou and Constantinides, 2004) and verified using ambient noise measurements from low-cost sensors located on each floor of examples of the buildings being studied and still installed within the town hall of Keffenach as part of an ongoing monitoring program. The fragilities of the URM buildings are, more or less, within the same range of damage and probability, while the TFM demonstrates a superior earthquake resistant nature, being less fragile for low and medium intensities.

With regards to the development of taxonomies, efforts were made to expand upon the idea of the faceted taxonomy, i.e., where specific attributes are defined, as in the GEM taxonomy, and then a correlation is made with more risk-specific taxonomies, such as that from HAZUS, where fragility curves have been defined for each class of structure. The risk-orientated taxonomies sees the typological clustering of structures with similar features. Hence a building of a specific class is expected to behave in a similar manner under given seismic loading. The developed methodology in Pittore et al. (2018) decouples the collection of observations of buildings from their assignment to a specific risk-orientated category in that the various faceted observations are combined and are assigned to one or more different categories by following a fuzzy scoring formulation.

The developed approach is based on a system where by the generic comparability of a given building, defined by some taxonomic description, with one or more pre-defined building classes. Each class has a series of attributes defining its structural (and relevant to the DESTRESS project, non-structural) characteristics, which are most relevant to that class. A weighing scheme is then employed, customized for each class, to adjust the importance of each attribute in terms of its contribution to seismic vulnerability. Note that such a scheme could, eventually, lead to a multi-hazard taxonomy scheme. A fuzzy scoring formulation is then used to assess the numerical scores using triangular fuzzy numbers, which is an array of three numbers representing the mode of the distribution, and the second and third representing the support of the fuzzy number, meaning the interval outside of which membership is zero.

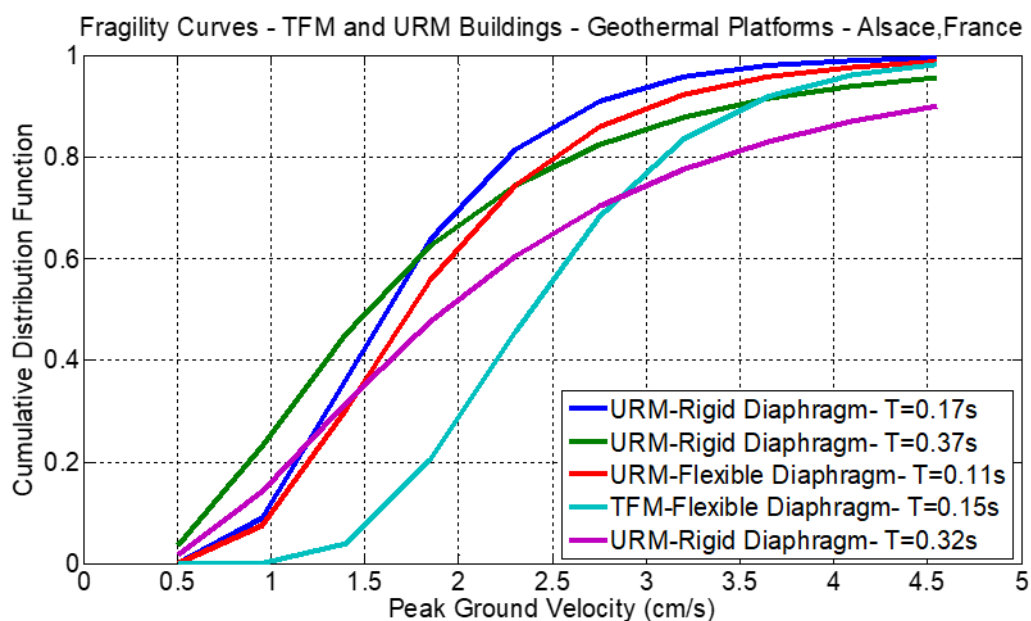


Figure 6 Proposed analytical fragility curves for first damage state (pre-yielding damage state –DS1-0.1% drift limit for non-structural damage) for URM and TFM buildings for the cases of structures near the geothermal platforms near Soultz-sous-Forêts, France (Megalooikonomou et al., 2018)

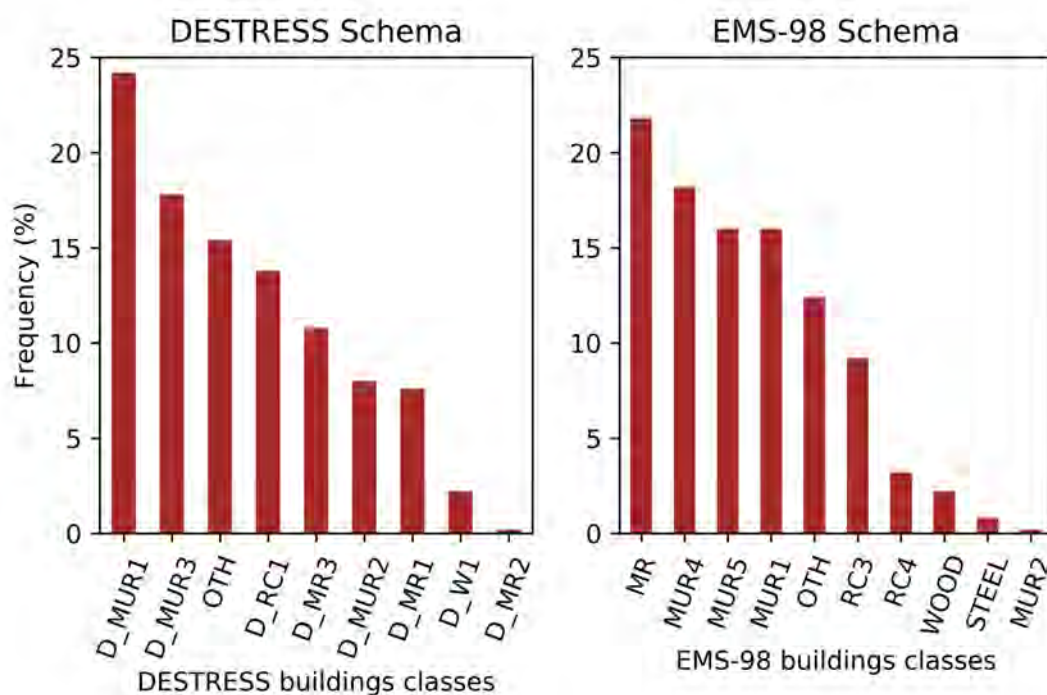


Figure 7 Result of the use of two different fuzzy mapping schemes applied to the building inventory collected in Soultz-sous-Forêts. The resulting exposure models are therefore based on the same information, but refer to two vulnerability schemas. The DESTRESS exposure/vulnerability model has been developed within the project considering the specific features of the residential buildings observed in-situ. The EMS-98 schema is a well-known classification proposed as part of the European Macroseismic Scale (EMS-98, Grünthal et al., 1988) and is largely used in risk applications, especially for unreinforced masonry buildings.

As in the work described above, the observations collected from the Soultz-sous-Forêts area are employed, and again using the faceted GEM taxonomy. This leads to class scheme for the study area, where the observations are mapped to the smallest number of classes, leading to the distribution of

building typologies and their association behaviour under seismic loading to be identified. The attributes in this case are, as discussed above, weighted. The employed weights differ depending on the attribute being considered. For example, attributes such as material type and material technology are fairly straightforward to observe, while being very relevant to seismic vulnerability.

Two resulting exposure/vulnerability models are shown in Figure 4. By applying two different fuzzy mapping schemes we can obtain different vulnerability models based on different classifications, either already existing or custom-tailored to the specific application.

In conclusion, several innovative methods were developed and expanded upon to allow a consistent and transparent modelling of exposure and vulnerability, as well as the effective and continuous monitoring of risk associated with possible induced seismic events. For exposure modelling, the employed fuzzy scoring technique allows the significant decoupling between the collection of observable structural and non-structural features of the building stock, and the assignment of risk-oriented building typologies that are related to specific fragility models. This technique has been applied to field observations gained from a survey that was carried out using the described RRVS platform. This resulted in several building classes deemed to be representative of the area's built environment. Those typologies have been considered for the development of specific fragility models which account for non-structural damage, under the assumption of the expected level of induced ground motion. An original hardware platform (MPwise) has been designed and tested within the same framework, including its installation in one building. All of these outcomes together provide the foundation for a risk monitoring and early warning system that could be easily tailored to specific regions and expected levels of ground motion. The modularity of this approach makes it particularly flexible and cost effective. A thorough validation of this methodology would require more time, given the very low level of seismic activity (induced or otherwise) within the test area.

4 Coda Wave Interferometry based monitoring techniques

4.1 Introduction

Deep geothermal projects based on EGS environments exploit geothermal resources in naturally fractured reservoirs. The economic viability of a geothermal project requires the development of the reservoir through stimulation campaigns which aim to improve the connectivity of these boreholes to the natural reservoir. The assessment of the productivity as well as the successful development and operation of deep underground heat exchangers necessitates the management of the risk, related notably to the potential seismic events produced by stimulation operations. This necessitates the use of relevant monitoring methods, enabling the fine-scale evolution of the reservoir to be followed, as fluid injections can also trigger non-seismic (or aseismic) displacements. Monitoring methods applied in reservoir management are generally based on micro seismicity. However, in order to constantly follow the reservoir's evolution, it is important to develop tools that apply independently of the spatiotemporally dependent seismicity.

The knowledge of the in-situ stress state is also of central importance to forestall the response of the rock mass to the different stimulation programs. Typically, the characterization of the stress tensor is derived from the analysis of borehole failures. For example, Azzola et al. (2019) analyzed Ultrasonic Borehole Imager (UBI) data acquired at different key moments of the Rittershoffen reservoir's development. The repetitive logging program conducted in the GRT-1 and GRT-2 wells of Rittershoffen permitted the study of the evolution of the stress state during the Rittershoffen geothermal project. However, the analysis generally relies on a single borehole image data set and information about the

evolution - interestingly allowed for the Rittershoffen project - is usually not available. The uncertainties in the stress magnitude, depending notably on the reliability of the strength parameter of the different lithologies, are also important and the choice of the rupture criterion is often uncertain. The limitations of such methodologies therefore make the study of the temporal evolution of the stress state difficult.

The past years has seen the emergence of passive monitoring methods based on Coda Wave Interferometry (CWI) (Snieder, 2006). These techniques aim at tracking small time delays in a diffusive medium from a direct comparison of waveform changes in the coda before and after a perturbation. The development of seismic noise correlation methods has contributed to the application of Coda Wave Interferometry techniques to permanent ambient seismic noise records. Indeed, it has been demonstrated that the cross correlation of ambient seismic noise recorded at two different receivers converge to the Green's function of the medium between the two stations (Campillo and Roux, 2015; Roux et al., 2005; Shapiro and Campillo, 2004). This makes the application of CWI techniques to compare stacked Ambient Noise Cross Functions (ANCFs) possible and opens up possibilities of monitoring the fine-scale evolution of the medium under assumption of the stability of the noise sources (for a complete review, see Campillo and Roux, 2015). These noise-based monitoring methods have been applied to many tectonic environments in recent years. Examples include the monitoring of volcanoes and mud landslides (Breguier et al., 2008, 2011; Duputel et al., 2009; Mainsant et al., 2012), and the geothermal reservoir in the area of Rittershoffen (Lehuteur, 2015; Lehuteur et al., 2014).

The application of such ambient noise-based monitoring techniques to the abundant data from the permanent seismic stations installed around geothermal plants offers the chance to monitor the evolution of deep geothermal reservoirs using a non-intrusive techniques. Past applications of Ambient Noise Interferometry (ANI) techniques showed that the methods could support reservoir management within various operational contexts, such as fluid injections or stimulation operations, by the development of a tool that enables the detection and location of the aseismic evolution within or around the reservoir. Obermann et al. (2015) shows for St Gallen, Switzerland, that a significant loss of waveform coherence is measured in the ambient seismic noise cross correlations, starting with fluid injections when other processes conducted by the operator in the wells didn't lead to such changes in the waveforms. These operations led to a significant gas kick and the closure of the deep geothermal project. The continuous monitoring of the deep geothermal reservoir from ANI measurements could have made it possible to anticipate such unwanted changes in the reservoir and may have avoided the closure of the deep geothermal project. Applied to the stimulation of the reservoir of the Basel geothermal project, such noise-based monitoring techniques were shown to provide important observables which are complementary to the results obtained with standard micro seismicity tools, and which could be applied to support the reservoir management (Hillers et al., 2015). In particular, Hillers et al. (2015) detected and located with ambient seismic noise an aseismic transient deformation induced by the 2006 Basel EGS stimulation which was not detectable with traditional micro-seismicity studies.

Ambient noise interferometry is thus a highly sensitive technique, but still suffers from problems with the interpretation of the measurements. Indeed, the physical processes at the origin of the CWI measurements are not clearly identified. Physically, the measurements are usually interpreted as small variations of seismic velocities, owing to different factors such as water table elevation variations, temperature perturbations, or changes in the stress state (Lockner et al., 1977; Planès and Larose, 2013; Snieder, 2002). Deformation is a contribution to the measurements that is generally neglected, as velocity changes are supposed to dominate the signals (Yamamura et al., 2003). Moreover, the measurements usually encompass all the sensitivity of the diffusive waves toward the multiple processes involved in the perturbation of the medium, which makes it difficult to decipher the different

contributions to the measurements. The study of the processes at the origin of the measurements is therefore of key importance. To address these open questions, our research activities aimed at a better understanding of the physical changes deduced from CWI, with a focus on the influence on interferometry measurements of the elastic deformation at the sample scale.

Our research activities focused on different aspects. At the laboratory scale, where the physical processes at the origin of the measurements can be easily managed, we focused on the forward modeling of the effects associated with the elastic deformation of the medium on the CWI. Our numerical model shows the strain influence on the time delays measured between the waveforms during the elastic deformation of the medium. To improve our understanding of the measurements, we get insights in the contribution to the time-delays measured from CWI techniques by comparing experimental results with those obtained in simulations replicating the experimental conditions. The focus is put on the signature on the CWI measurements of the elastic mechanical and thermal deformation of the sample. In both cases, the numerical model replicates the mechanical and acoustic behavior of the laboratory experiments. Finally, our results allow us to question at the laboratory scale the processes at the origin of the delays and of the loss in coherence measured between the waveforms.

Finally, by upscaling the representation of a strongly diffusive propagation medium proposed hereby, we propose a numerical model contributing to the interpretation of the temporal variation of the ANI measurements obtained in the vicinity of Rittershoffen. Surface temperature and water table elevation changes are identified as the possible cause of the trend highlighted in the frequency range considered in our approach, i.e., [1-3] Hz. From the modeling of the time-series, we propose a phenomenological interpretation of the measurements which contributes to removing unwanted effects in the monitoring. As natural surface phenomena unrelated to the reservoir evolution could induce potential bias in the monitoring of the evolution of the geothermal reservoir, we address the applicability of such passive techniques for the monitoring of unexpected changes in the deep geothermal reservoirs, numerically.

4.2 Analysis of the time-delays measured during the elastic deformation of the sample, at laboratory scales

Laboratory experiments combined with numerical simulations are essential for the physical interpretation of CWI measurements. The interpretation of laboratory measurements, in terms of disruptive events, is challenging since the measurements usually enclose at once all the contributions of the various physical sensitivities of the scattered waves. Deciphering a specific effect remains difficult from an experimental approach. We focus here at the laboratory scale on the elastic deformation of the sample induced by the mechanical and thermal perturbation of the sample. As the physical properties of rock in deep geothermal reservoirs are non-trivially influenced - at all scales- by changes in temperature and pressure, laboratory experiments on representative samples and the forward modelling of the involved processes are necessary to develop relevant seismic monitoring techniques by improving our understating of the related measurements.

4.2.1 Mechanical deformation of the sample

- Modelling of the Mechanical Strain Influence on Coda Wave Interferometry

This section includes a comprehensive description of the results published by Azzola et al. (2018b). We address here the signature of the wave diffusion and in the CWI measurements of the elastic and reversible deformation of the sample. We compare an experimental approach and numerical

modelling, with both including the same two parts: seismic wave scattering, and mechanical deformation obtained from the step-by-step displacement applied at the top of the sample. The aim is to develop a comparative modelling of the effect of stress changes (from 5 up to 50 MPa) in the elastic regime during a uniaxial compression test on the CWI measurements. The mechanical loading is a step by step rigid displacement of the upper face of the sample (see Figure 5). With each step the displacement is increased, a wavelet is sent through the medium (left insert of Figure 5) and the waveforms recorded (right insert of Figure 5) are compared sequentially using CWI techniques.

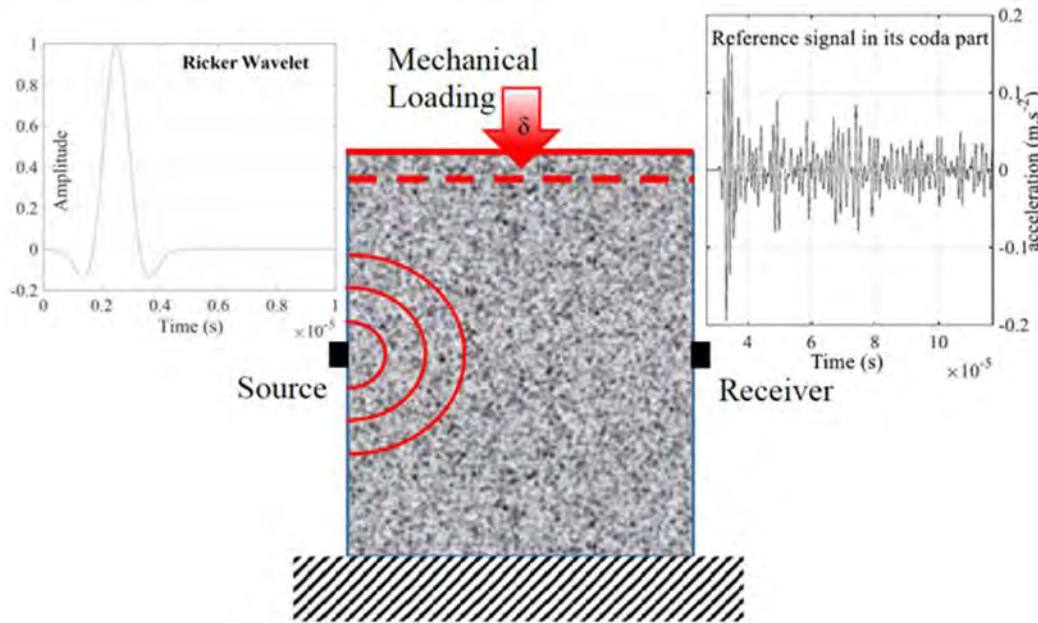


Figure 8 Principle behind the numerical experiment. We impose a mechanical loading to a numerical sample imposing a rigid step-by-step displacement δ to its upper face. During the loading, a Ricker wavelet (see left insert) is sent in the medium from the source and recorded at the opposite face by the receiver (see right insert). The waveforms are recorded for 32 positions of the receiver equally distributed along the right-hand boundary of the sample.

The experimental method (see Figure 6 for a detailed representation of the experimental apparatus) consists of a uniaxial load of an ab-initio designed scattering block of Aluminum 2017A (Au4G), commonly labelled Duraluminium, during the time-lapse recording of the elastic wavefield.



Figure 9 Image of the experimental apparatus. The piston of a servo controlled 10 T press loads a holed block of Au4G (70 holes of radius 3 mm). Two linear acoustic arrays of 32 sensors are held in direct contact with the boundaries of the sample.

At each step of the displacement imposed by the piston, the element of the transducer on the left which is located at the middle of the array sends a pulse wave. This wave is recorded by each of the 32 elements transducer located on the opposite face of the sample. An image correlation technique is used to estimate the displacement field by comparing pictures of the sample taken at each step of the loading procedure.

In order to test the partitioning between the different physical phenomena in question, we combine both the elastic deformation and the seismic wave propagation modelling, in which parameters and disruptive elements are easily managed. The elastic deformation is obtained from a finite element approach (Code_Aster). We perform a direct numerical modelling of seismic wave propagation within the sample using a spectral element approach (SPECFEM2D) during its deformation (Komatitsch and Vilotte, 1998). It enables us to observe the evolution of the synthetic waveforms of the scattered waveforms during the deformation of a similar numerical sample with the same geometry and properties. It therefore allows a detailed comparison between both approaches to be made. The numerical modelling enables us to focus, all at once or in a distinct way, on the signature of the relevant phenomena involved during the elastic and reversible deformation of the sample: a) of the sample and the scatter deformation without intrinsic wave velocity variations, b) of the local density changes due to local volumetric strain, and c) of acousto-elastic effects due to non-linear elasticity (Hughes and Kelly, 1953; Murnaghan, 1951).

- Results – strain influence on delays measurements

A first result of our analysis is the good agreement between the mechanical and acoustic behaviour of the laboratory sample and its 2D representation considered in the simulations (Figure 7).

We characterize the scattering behaviour by measuring the temporal variation of the seismic energy. We show a good agreement between the temporal variation of the seismic energy measured in both media (see panel a) of Figure 7). The mean free path, which is the mean distance between two successive scattering events, is key information for characterizing the scattering behaviour of samples. The mean free path in the laboratory and numerical samples are inverted by comparing the energy

density function (plain black and red curves in panel a) of Figure 7, respectively) with a simple multiple diffusion model by a least square fitting procedure. The best fit to the laboratory and numerical measurements (respectively black and red dashed lines) determined by the least square regression are presented in panel a) of Figure 7.

The good agreement between the mean free path estimated from both measurements also contributes to assessing the similarity in the acoustic behaviour of the numerical and the laboratory sample.

The mean free path estimated in both media are shown to satisfy the conditions necessary for the establishment of strong scattering regime needed for the CWI analysis (Planès and Larose, 2013).

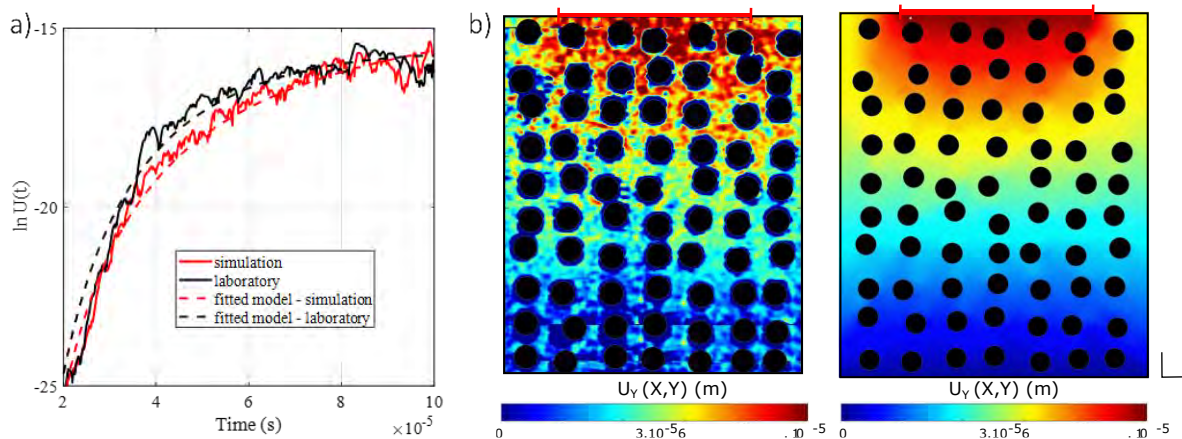


Figure 10 a) The logarithmic and normalized expression of the energy density, $\ln U(t)$, is computed with measurements obtained in the laboratory (plain black curve) and in the simulation (plain red curve), in an unstressed medium. The 32 functions computed from records obtained at each sensor of the receiver line are averaged spatially. The best fits to the laboratory and numerical measurements, determined by the least square's regression to estimate the mean free path, are plotted as dashed curves (respectively dashed black and dashed red lines). b) experimental displacement field $u_Y(X, Y)$ calculated from image correlation between a picture of the unstressed sample and one captured after imposing a displacement of $\delta = 60 \mu\text{m}$ to the top of the sample (corresponding to an applied force of $F = 75 \text{ kN}$). c) Numerical displacement field $u_Y(X, Y)$ computed by Code_Aster when applying the same loading and using the same color scale. The holes introduced in the sample are represented by black circles with the same size and spatial locations. The red bar indicates the extent of contact zone between the sample and the piston.

We also provide evidence showing the linear elastic behaviour of the propagation medium, as well as the similar linear behaviour between applied displacement and measured stress, for the numerical medium and for the laboratory sample. The multi-scale comparison of the displacement measurements, i.e., the comparison of the spatial distribution of the local displacement field measured in the numerical case and in the laboratory experiments (see panel b) of Figure 7) as well as the comparison between vertical macroscopic behaviors, shows that the mechanical behaviour of the numerical sample reproduces that of the laboratory sample.

The verifications of these hypotheses, related to the framework of the study, legitimize our procedure and allows the comparison of the CWI measurements. First, we show that the wavefield propagated is sufficiently diffracted to show the appearance of time shifts between the waveform recorded at a given loading state and a reference one, in their late parts (see Figure 8, with numerical records). These time shifts, dt , are quantified by comparing sequentially the waveforms acquired using CWI methods. The methods aim at measuring the relative variation of delays with time in the signal, dt/t .

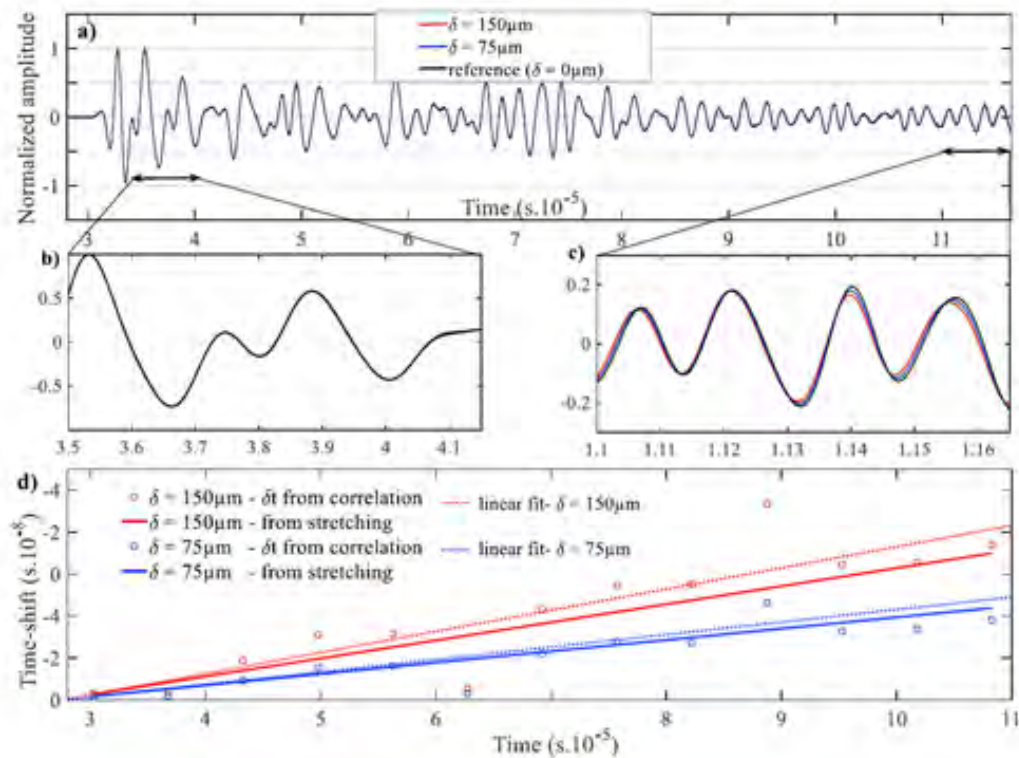


Figure 11 Coda wave interferometry. a) Comparison of three synthetic waveforms recorded respectively for an imposed displacement $\delta = 0 \mu\text{m}$ (black), $\delta = 75 \mu\text{m}$ (blue), and $\delta = 150 \mu\text{m}$ (red); b) zoom in a $6.5 \mu\text{s}$ window of the waveform at the beginning of the coda where a negligible time shift is observed and c) zoom at the end of the waveform where the time shift is clearly sensitive to the imposed displacement. d) Time shifts within the coda measured with either a time window correlation technique (circles) or a frequency stretching technique (solid line) when comparing waveforms at 75 and $0 \mu\text{m}$ displacement (blue) and at 150 and $0 \mu\text{m}$ displacement (red). The lines fitted on the time shifts measured by a time window correlation technique (circles) allows the relative time shift $\delta t/t$ to be measured.

The increase of the relative time shift with strain shows that elastic deformation is fully correlated to time shifts. Our tests show that the time shifts measured in the seismograms carry a real deformation signal and are not numerical artefacts. We show that the evolution of the relative time delays with the applied stress highlighted in the laboratory and in the numerical model are consistent (respectively the black and red curves entitled “model 1” in Figure 12).

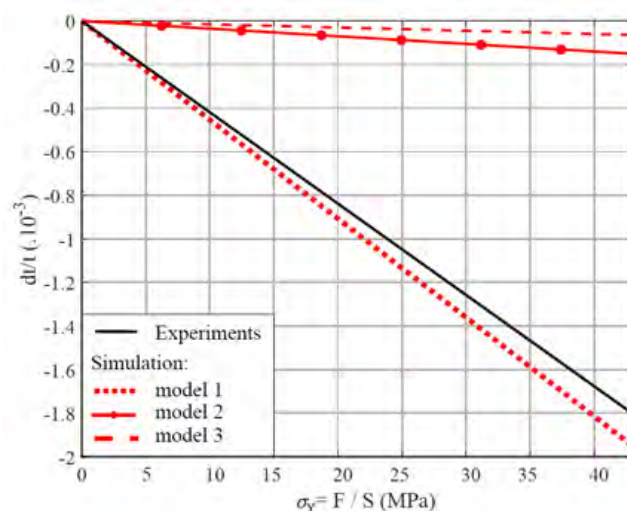


Figure 12 Comparison between the linear regression fitted to the time shifts dt/t of the laboratory experiments (black line) and the ones obtained from simulations based on three distinctive models as a function of the stress σ_Y . The red dotted line (model 1) depicts the measurements when modelling all the influences on dt/t of: the change in the sample shape, the change in the wave velocity variations due to density variations, and those due to acousto-elastic effects using the third-order elastic coefficient (TOEC) of aluminum. Model 2 corresponds to the relative contribution of the change of sample shape including the boundaries of the holes (i.e., the scatters) (red plain line). Model 3 is an extended version of Model 2 with also the wave velocity variations due to density variations (red dashed line). Relative time shifts are the mean values calculated from the 32 distinctive estimates obtained along the receiver array.

When modelling distinctly the contribution of the relevant phenomena included in the model, our numerical measurements show the dominant influence of non-linear acousto-elastic effects on the scattered wavefield and subsequently on the CWI measurements. Indeed, when modelling CWI measurements without these acousto-elastic effects, i.e., with only the impact of the deformation of the sample boundaries and of scatterers, only 11% of the relative time delays measured in the laboratory are numerically reproduced (see model 2 in Figure 12). Adding the contribution of the density change related to the volumetric strain almost lowers the magnitude of the relative time delays dt/t measured through the simulation (see model 3 in Figure 12).

Our numerical model therefore identifies a strain sensitive signal. By comparing the signature on wave scattering of different physical phenomena involved in the reversible elastic deformation of the sample, we have gained insights in their relative contribution to the CWI measurements. Our results open new perspectives for the interpretation of CWI measurements that could have implications for the monitoring of infrastructures or natural geological structures (e.g., fractured reservoir, porous medium).

4.2.2 Thermal deformation of the sample

This section consists in a comprehensive description of the results published by Azzola et al. (2018a).

- Purpose

Understanding the influence of temperature changes on the physical and mechanical properties of reservoir rocks is an important issue for the monitoring of deep geothermal reservoirs such as Enhanced Geothermal Systems (EGS). We also quantified the impact of thermo-elastic deformation on CWI measurements by comparing experimental results obtained from a previous study on Westerly Granite to a numerical approach aiming at modelling wave propagation in complex media during thermo-elastic deformation.

- Principle of the experiments / the numerical modelling

The experiments of Griffiths et al. (2018), whose laboratory apparatus is sketched in Figure 10, aim at monitoring non-permanent and permanent effects, i.e., thermos-elastic effects and thermal micro-cracking on a Westerly granite sample when it is heated and cooled from room temperature to a maximum temperature of 450°C in three successive cycles, as presented in panel b) Figure 10. Westerly Granite was chosen as it is well-studied, and its physical and mechanical properties are well-known, near-isotropic. The crystal assembly of Westerly Granite is similar to the so-called “fine-grained two-mica granite” of Soultz-sous-Forêts (e.g., Hooijkaas et al., 2006). Waveforms were compared iteratively by CWI during each cycle. If large and mostly permanent changes in the waveforms were measured during the first cycle, the following cycles show further but reduced velocity reduction.

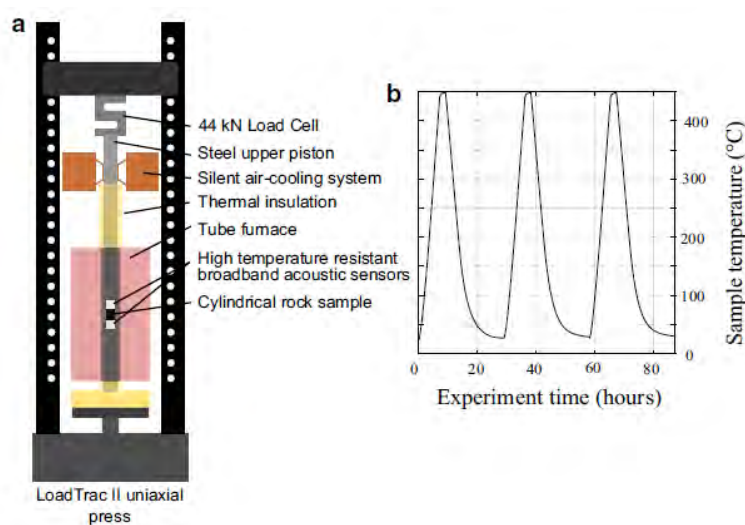


Figure 13 a) Sketch of the experimental setup (modified from Griffiths et al. 2018) for wave velocity measurements on a Westerly Granite sample. The apparatus consists of a uniaxial press, a tube furnace and for waveform measurements, a pair of high temperature resistant and broadband acoustic sensors that are set in direct contact with opposing ends of the sample [see Griffiths et al. (2018) for details]. Upper acoustic sensor is the source and the lower one is the receiver. b) Evolution with time during three heating/cooling cycles, of the temperature measured at the center of the sample with a thermocouple inserted into a hole drilled radially.

The laboratory experiment is transcribed in the numerical scheme. The forward modelling approach enables to highlight the contributions of various physical processes (velocity changes, heterogeneity of the elastic deformation field, amplitude variations, etc.) on CWI measurements. The modelling approach combines a spectral element approach (SPECFEM2D) to study the seismic wave propagation within a diffusive medium, while elastic deformation of the medium is modelled using a finite element code (*Code_Aster*).

- Results

An important simplification of the numerical modelling is the definition of a homogeneous sample with representative elastic moduli and thermal expansion coefficient but where scattering is only obtained from multi-reflections on the boundaries. We show that multiple reflections on the boundaries of our simplified numerical sample reproduce well the wave scattering properties of the experimental granitic sample characterized by a complex mineral assembly and a large set of micro-cracks. We based

our comparison on the temporal variation of the seismic energy that describes the scattering behaviour of both the experimental and the numerical samples (see Figure 11).

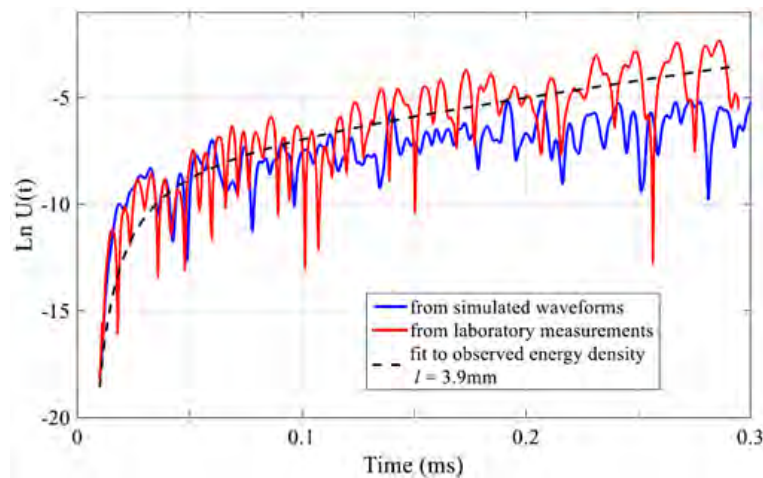


Figure 14 The logarithmic and normalized expression of the energy density $\ln U(t)$, represented both in the experimental case (red line) and in the simulated case (blue line), characterizes the scattering properties and is used for the linear inversion of the mean free path. The comparison of both functions shows that the numerical medium reproduces the wave scattering happening in the experimental sample. The dashed black line corresponds to the best fit to the laboratory measurements using the diffusion model and leading to an estimate of the mean free path $l = 3.9$ mm.

We also show that both samples share a similar thermo-elastic behaviour, but only after the first heating and cooling cycle. In the simulation, when we assume that the coefficient of thermal expansion, the bulk modulus and the Young's modulus are constant with temperature, the two main results are as follows:

- The isotropic thermal expansion of the medium is retrieved from the relative variation of delay dt/t measured in the simulation with temperature (Figure 12). CWI results obtained from the simulation in a homogeneous 2D rectangular sample consist of a deformation signal, due to the elastic and homogeneous deformation of the sample.
- The comparison with the CWI signal measured under comparable conditions at the laboratory shows that the relative variation of delays dt/t measured in the simulation are significantly lower (12 times) than in the simulated experiments, as depicted by the slopes of the linear regression fitted to simulated and laboratory CWI results (Figure 12). In the experiments, and in the absence of microcracking (i.e., during cycles 2 and 3), deformation alone only partly explains the impact of temperature changes on CWI measurements.

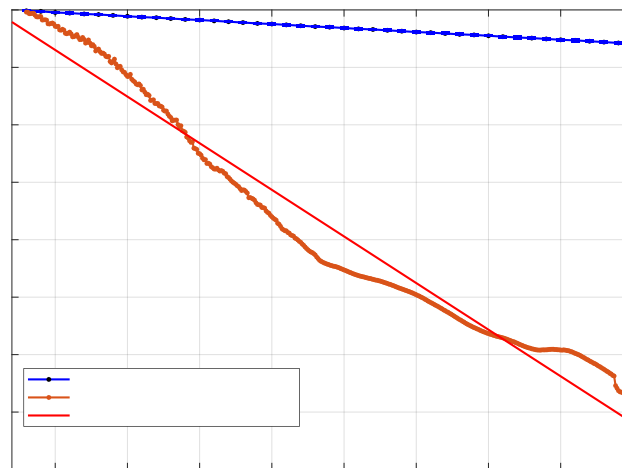


Figure 15 Comparison of simulated and laboratory CWI measurements. We represent the CWI measurements obtained in the laboratory (orange line) during the second heating cycle of Westerly Granite and in the simulation (blue line) with temperature measured at the middle of the sample. Relative time delays are measured by comparing the waveform recorded at a given temperature with respect to the “reference” waveform. A linear regression is fitted to the measurements to estimate the slopes -0.13×10^{-4} to numerical results and -1.62×10^{-4} to laboratory measurements (blue line and red line, respectively).

We finally discuss the role of irreversible deformation for the observed discrepancy by introducing temperature dependence of elastic moduli in the model. The CWI results obtained in the experiments are better modelled by complementary simulation in which the contribution to the CWI measurements of the temperature dependence of E and K are added (results are presented in Figure 13). The CWI measurements overestimate the experimental results obtained during cycle two and three, because they include partial thermal damage microcracking that are less important in the experimental results, in cycle 2 and 3. On the other hand, the intact sample is subject to large velocities perturbations during the first cycle, retrieved in the simulation from the time dependence of the density, Young’s modulus and bulk modulus.

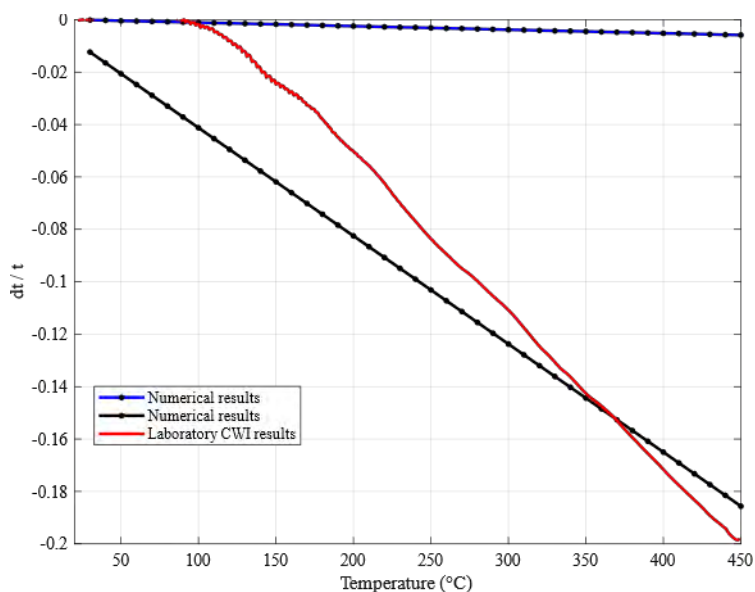


Figure 16 Comparison of laboratory CWI measurements during the first cycle (red line) with the simulated CWI measurements obtained without (blue line) and with (black line) introduction of a dependency with temperature of the bulk modulus K and of the Young’s modulus E . A linear regression is fitted to the measurements. The slope of the linear regression fitted to the

simulated CWI results is -0.13×10^{-4} without introduction of the temperature dependency and it is -4.1×10^{-4} when the dependency is added to the simulation.

Our measurements bring new perspectives for the discrimination between the different effects induced by thermal variations— changes of properties, such as velocity, attenuation, anisotropy, and scattering properties—deduced from CWI signals. The interferometry technique shows to potentially detect stress changes linked to a reservoir thermal variation during stimulation or exploitation which could help to guide stimulation strategies designed to optimize reservoir productivity.

4.3 Temporal and spatial variability of decoherence during the elastic deformation, at the laboratory scale

The simulations and laboratory measurements presented to study the strain influence on the CWI during the mechanical elastic deformation of the Duraluminium (Au4G) sample, illustrate complex interactions between several physical processes. In addition to the delays measured between the waveforms we also measure a loss of coherence (decoherence) between the waveforms (for example, see Figure 8), even if the difference in the shape of the seismograms is slight. Both theoretical and experimental results have shown that decorrelation measurements are related to changes in the diffusion properties of the medium and thus to structural changes in the medium (e.g., Larose et al., 2010; Michaels, 2008; Rossetto et al., 2011). The understanding of the physical processes at the origin of decoherence and time shifts necessitate a more complete analysis of the waveforms acquired during the elastic deformation of the Au4G sample in the laboratory and in the simulations. We analyzed the spatial and temporal variability of the delays and of the decoherence measured during the experiments and the in the simulations.

4.3.1 Temporal and spatial variability of delays and decoherence measurements

We measured delays and decoherence by comparing the waveform acquired at a given stage of the loading procedure to the reference one, using a time window cross-correlation method: the time-windows centered at time t in the waveform are cross-correlated to the time window in the reference signal in order to evaluate the time delay and the loss of coherence at times t in the signal. The method, which is repeated at distinct times along the signal, was introduced in Poupinet et al. (1984) and further developed in Snieder (2002). We consider here a 32-sensors long receiver line which faces the source, i.e., deployed along the right face of the sample (see Figure 1). The method is replicated for each recorded signal. It enables to study both the spatial and temporal variability of the measurements.

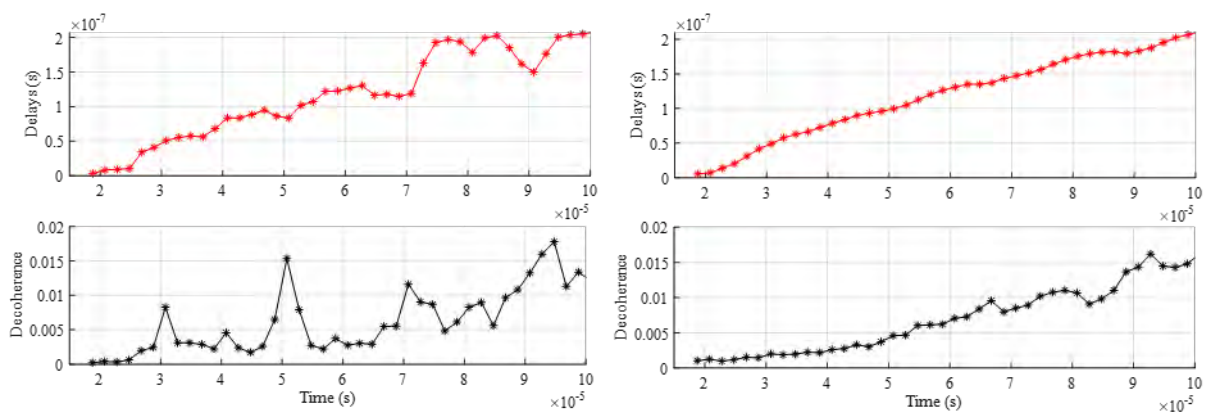


Figure 17 Delays (red) and decoherence (black) with time in the signal, measured in simulations during the elastic deformation of the sample due to a 75µm displacement of the upper face of the sample. The measurement, obtained in overlapping

windows $6.5\mu\text{s}$, is obtained at middle sensor of the receiver line (left) or is spatially averaged over the 32 sensors of the receiver line (right).

We show that both decoherence and delays are measured during the elastic deformation of the sample (Figure 14). We analyze first spatially averaged measurements: delays and decoherence measured at a given time in the signal are averaged over all the position of the receiver in the receiver line (see right part of Figure 14). For a given loading state, both measurements increase in a linear way with time in the coda. But the delays and decoherence measured at the sensor located at the middle of the line (see left part of Figure 14) shows more variability, with different sensibilities for each measurement. It suggests that both measurements are impacted locally in a different way.

We then study the spatial variability, along the receiver line, of the mean delays and decoherence: the delays and decoherence measured at time t in each successive window along the signal are averaged to highlight the variability of a single measurement along the receiver line. For a fixed displacement ($\delta=75\mu\text{m}$ is applied at the top the sample), we compare the decoherence and delays measured in the simulation and laboratory experiments in Figure 15.

The measurements are compared to mechanical observables, obtained from Code_Aster, in order to decipher the specific sensibilities of the delays and of decoherence.

From Figure 15, we show that delays are sensitive to the volumetric strain: we show a strong correlation between the variation of time delays, averaged with time, with the position in the receiver line and the volumetric strain measured using Code_Aster. On the other hand, the decoherence averaged over time follows the spatial variability of the displacement. The measurement is sensitive to the zone of loading of the sample, where changes in the scattering properties of the sample are expected to occur.

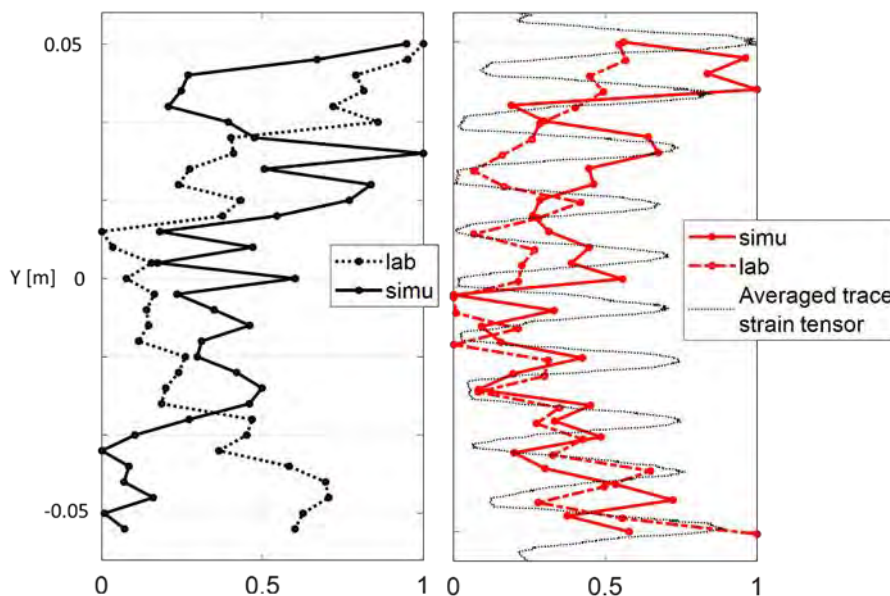


Figure 18 normalized values of temporally averaged decoherence and delays (respectively black and red; measurements in successive windows in the signal are averaged at each sensor of the receiver line) with position along the right boundary. The measurements obtained in the simulation (plain line) and in the laboratory experiments (dashed line) are compared to the

volumetric strain, averaged horizontally and measured using Code_Aster, to investigate the spatial variability and the sensibilities of both measurements.

4.3.2 Numerical analysis of the sensibility of delays and decoherence measurements

From numerical experiments, we investigate the specific sensibility of the delays and decoherence toward volumetric strain and displacement, respectively. We consider two numerical simulations in which the position of one of the 70 round scatterers of the numerical sample is shifted by $75\ \mu\text{m}$ following two distinctive approaches. The “perturbed” medium is obtained either by applying directly the displacement to the mesh grid and by discretizing the mesh grid again (see Figure 16.a.), or by applying the displacement as a boundary condition in the resolution of the mechanical problem by Code_Aster (see Figure 16.b.).

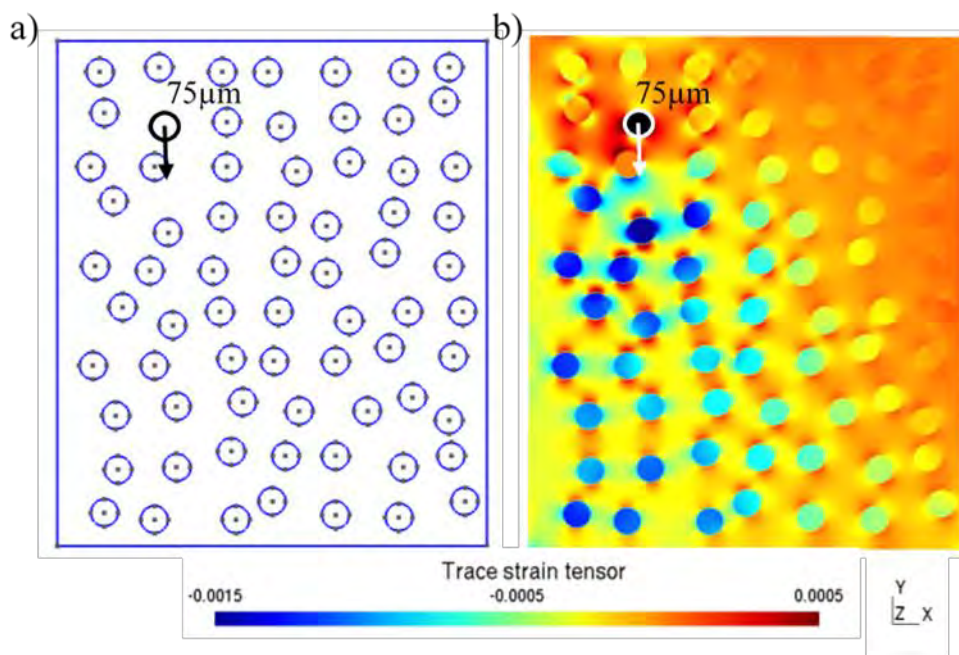


Figure 19 Principle of the experiments where a $75\ \mu\text{m}$ displacement is applied to the boundary of one of the 70 round scatterers in two different ways. a) The perturbed medium is obtained by shifting the position of the round scatterer by $75\ \mu\text{m}$ in the mesh grid before it is discretized again. b) The perturbed medium is obtained by deforming the mesh grid using Code_Aster. The homogeneous displacement of $75\ \mu\text{m}$ is a boundary condition in the mechanical problem.

We show that delays are particularly sensitive to the volumetric deformation (left part of Figure 17), when the displacement is applied as illustrated in panel b) of Figure 16. When the displacement of the scatterer is applied as a boundary condition of the mechanical deformation of the sample, the mesh grid will deform consequently. Volumetric strain is estimated from the trace of the strain tensor.

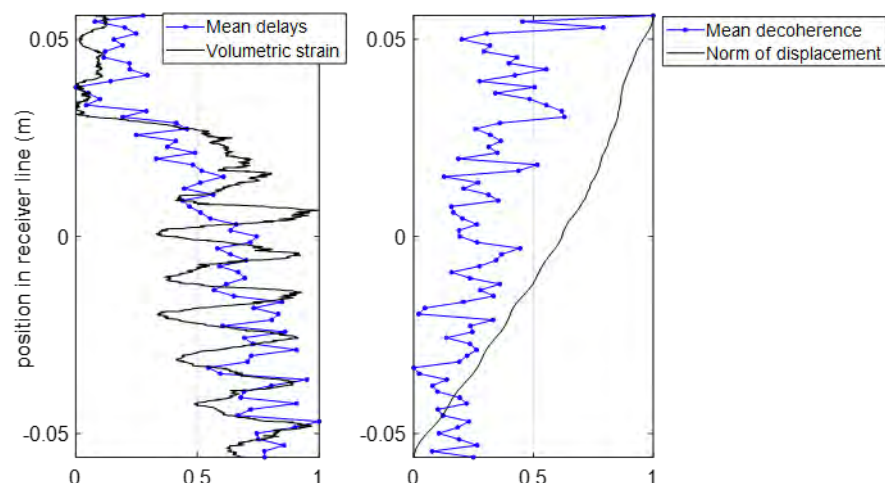


Figure 20 The spatial variability of delays (left) and decoherence (right), averaged temporally in the signal length and normalized, are measured with the position of the sensor along the receiver line (blue dotted line). The displacement (black line, right) and the volumetric strain (black line, left) are measured within the sample by Code_Aster, the latter being estimated from the trace of the strain tensor. The measurements are averaged horizontally.

In a different way, if the displacement of the scatterer is applied geometrically, as illustrated in panel a. of Figure 16, the mesh grid will be strongly impacted in a local way. Delays evolve noisily and their magnitude is two order of magnitudes lower than in the previous case. The decoherence and the norm of the displacement evolve together with position along the side of the sample. Decoherence measurements are particularly sensitive to zone where strong change in the mesh grid are applied and where the scattering properties of the medium are expected to be modified consequently.

The results of our numerical analysis outline that decoherence measurements are related to structural changes happening in the medium where the displacement is applied. We observe that delays are strain sensitive. The spatial variability of delays and of volumetric strain are strongly correlated.

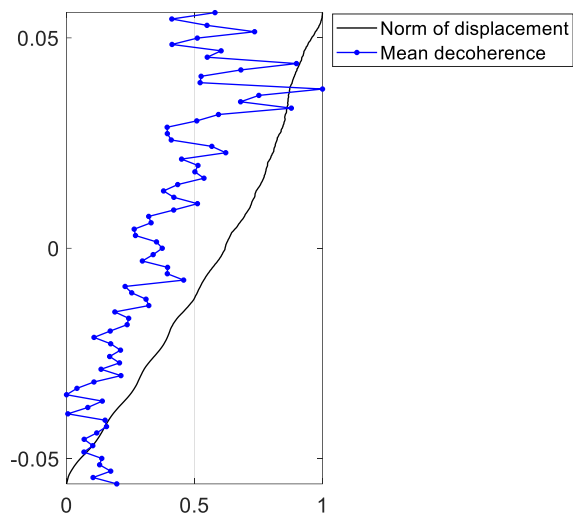


Figure 21 The spatial variability of decoherence, averaged temporally in the signal length and normalized, are measured with the position of the sensor along the receiver line (blue dotted line). The norm of the displacement (black line) is measured within the sample and averaged horizontally.

4.4 Upscaled numerical model

The studies conducted at the laboratory scale and their results leads us to consider an application at the scale of the reservoir to study the applicability of monitoring techniques based on the ambient noise to follow the evolution of the reservoir in various operational contexts.

4.4.1 Purpose of the approach

The RT seismic network deployed around the Rittershoffen and Soultz-sous-Forêts geothermal plants records passively since 2012 (Figure 19). Ambient noise based techniques have been applied to this abundant dataset in time for the entire period of availability of seismic network recordings.

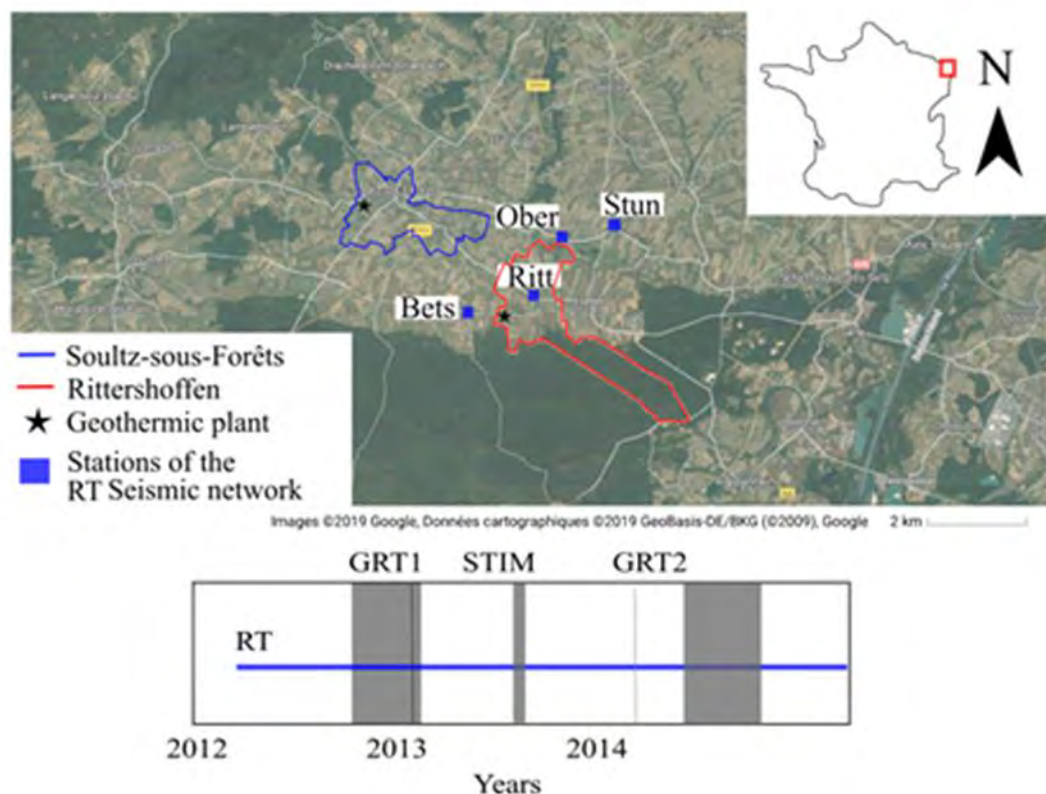


Figure 22 Overview of the localization of the Rittershoffen and Soultz-sous-Forêts EGS projects, in the upper Rhine Graben, as well as an overview of the RT seismic network deployed in the vicinity Bottom: data availability over time for the RT network. The grey periods noted “GRT1” and “GRT2” correspond to the drilling periods of the wells at the Rittershoffen site and “STIM” corresponds to the stimulation of the GRT1 well.

When the data are filtered in the [1-3] Hz range, the time-series of the CWI measured between stacked ANCFs shows a clear annual trend, replicable from year to year. This specific trend is highlighted in panel a. of Figure 20 from the monthly stacked data. The physical processes at the origin of the trend are not well understood. The filtering band as well as the reproducibility of the measurements suggests that natural surface phenomena, acting at shallow depth and strongly reproducible, are at the origin of the measurements. Surface temperature and water table elevation variations (panels b) and c) in Figure 20) are among the natural phenomena showing such a reproducibility from year to year. But these natural processes could also bias the monitoring of the reservoir evolution: the applicability of ambient noise-based techniques to support the reservoir management in various contexts (fluid injection or stimulation operations, for example) necessitates that the contribution of the change in the reservoir can be distinguished from the contributions of natural surface phenomena. The identification of the processes at the origin of the measurements is important to better our understanding of the time series measured but also to open perspectives for the removing of such unwanted effects in the reservoir monitoring.

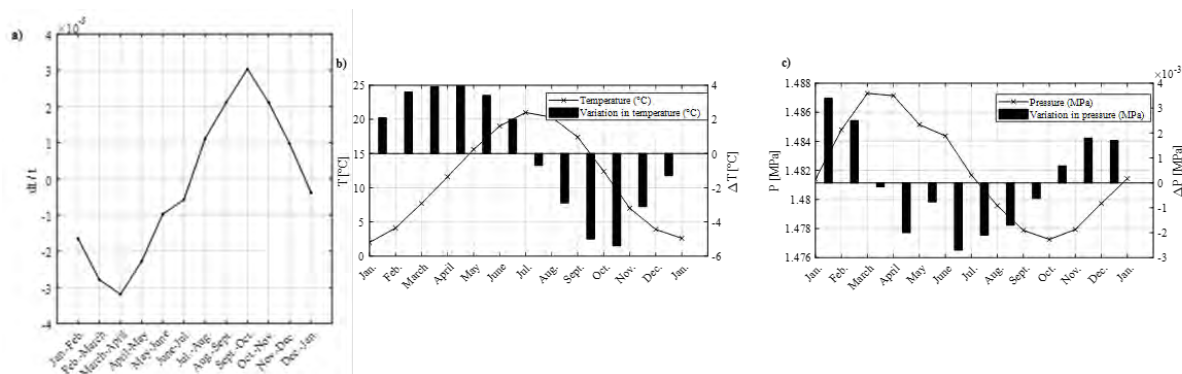


Figure 23 a): time series of the optimum stretching coefficient for the North components of RITT and BETS, filtered between 1 and 3 Hz, and stacked monthly for the period from 2012 to 2017. b) and c): Annual surface temperature (lefts) and water table elevation converted into pressure (right) presented in absolute values (line) or in terms of monthly variations (bars). The mean surface temperature is measured monthly in Rittersshoffen. The water table elevation is measured weekly at the nearby Haguenau hydrological station. The measurements are stacked monthly for the period from 2012 to 2017 and converted into pressure.

4.4.2 Principle of the numerical modelling

To get insight in the process at the origin of these measurements, we upscaled the representation of a strongly diffusive medium proposed previously at the laboratory scale and developed a numerical model aiming at modelling the stacked time-series measured in the vicinity of the Rittersshoffen project (Baujard et al., 2017). The numerical sample is a 2D representation of a geological section of the geothermal reservoir, made of thick granitic layer overlain by a thin sedimentary layer (Figure 21). The medium shows large round asperities behaving as numerous scatterers which create a strong impedance change between the bulk and the inclusions. We combined the thermo-elastic deformation of the sample resulting from the variation of surface temperature and of water table elevation using a finite element approach (Code_Aster), to the simulation of the wave propagation using a spectral element approach (SPECFEM2D). The one-year loading procedure is discretized in successive stages of one month.

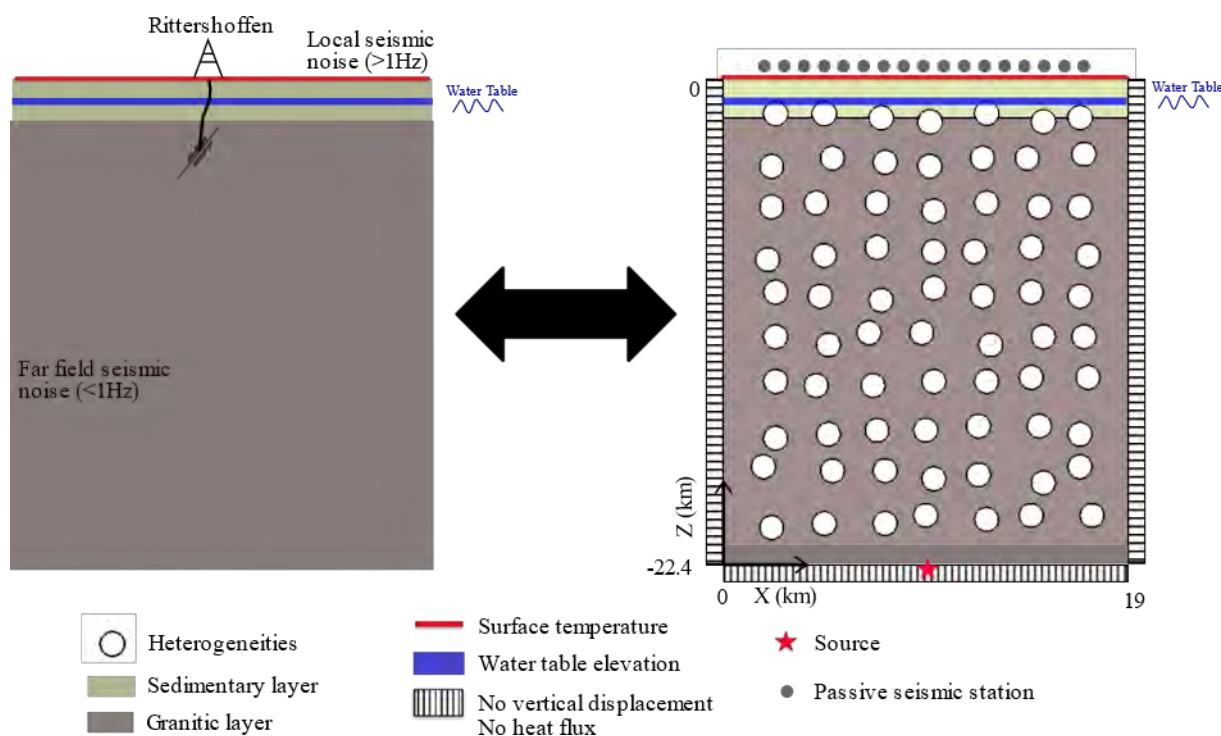


Figure 24 Principle of the numerical model developed to model the signature on the interferometry measurements of annual surface temperature and water table elevation variations and local changes within the reservoir. The sample consists in a 2D representation of a geological section down to 22.4km under Rittershoffen, in which the boundary conditions for the deformation modelling (i.e., surface temperature and pressure variations) act superficially and the deep part with large heterogeneities aim at scattering the wavefield propagated from the source in the seismic propagation modelling.

The numerical model models the impact of the annual variations in surface temperature and water table elevation measured in the vicinity of Rittershoffen. These perturbations, which are applied at the top boundary of the sample, act mechanically at shallow depth. The significant depth of the numerical model and the dense population of asperities (Figure 21) intends to strongly scatter the wavefield in order to retrieve the same scattering conditions in the numerical model than with the ambient noise recorded in the vicinity of Rittershoffen. In addition to model the signature on the CWI of the ambient noise cross-functions of annual perturbations in water table elevation and surface temperature, the numerical model aims also to study the influence of a local perturbation in the reservoir, which could potentially be related to a transient deformation in the reservoir. We model here a local increase of pressure (1, 10 or 100 MPa) in a kilometric asperity.

4.4.3 Results

We show first that the scattering properties deduced from the ambient noise recorded in a pair of stations in the vicinity of Rittershoffen, is retrieved in the numerical model (Figure 22). We base our comparison on the measure of the temporal variation of the seismic energy and on the estimation of the mean free path from a least square regression comparing the measurement to a simple diffusion model.

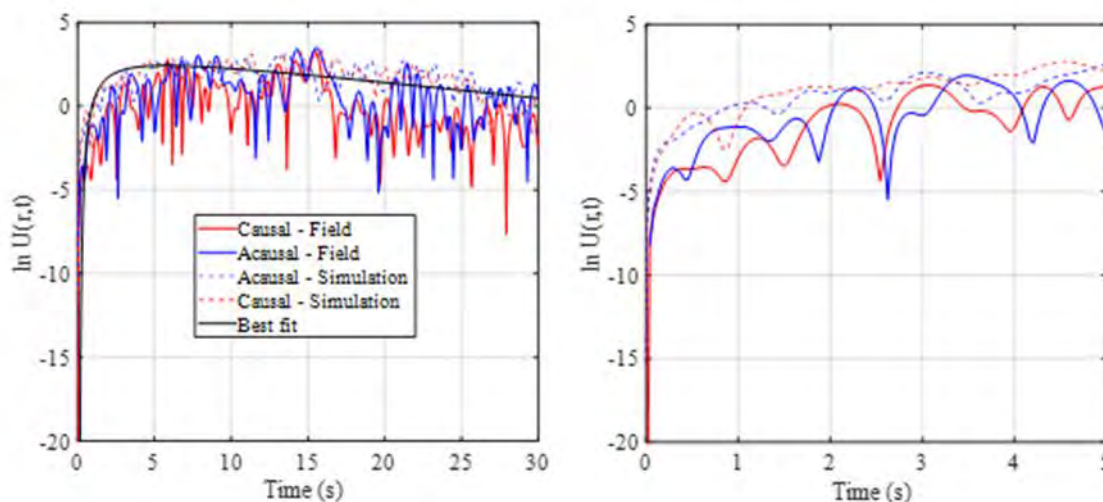


Figure 25 The scattering properties are characterized from the measurement of the temporal variation of the seismic energy using the cross-functions of the north components of the RITT and BETS stations (dashed line), and from the cross-functions measured in the simulation (plain line). We show a logarithmic and normalized expression of the energy density, measured with the causal (red) and acausal (blue) part of the cross-function, enabling to estimate by least square regression to a diffusion model, the mean free paths. Black line shows the best fit determined by the least square method.

Also, the cross-functions measured from the waveforms recorded following the emission at the punctual source of dominant frequency of 2 Hz are with a spectral content similar than the ANCFs deduced from ambient noise recordings.

We show that the time series measured from the North component of the RITT-BETS station pair, operating in the vicinity of Rittershoffen, is retrieved in the numerical model (black and red curves in Figure 23 respectively). The time series is correlated to the annual variation in water table elevation. Considering the similarity of the approaches and the good agreement between the annual variations measured in the simulations and infield, we show the preponderant influence of water table elevation variations on the annual time series deduced from ambient noise records in the vicinity of the deep geothermal reservoir exploited in Soultz-sous-Forêts and Rittershoffen.

The identification of the processes at the origin of the interferometry measurements opens perspectives for the removing of unwanted effects in the monitoring of the reservoir. Such natural phenomena, unrelated to the reservoir evolution, can induce potential bias in the monitoring of the reservoir evolution, at short term. We show that an unexpected change in the deep geothermal reservoir, such as a local increase in pressure, could be monitored from such ambient noise based passive monitoring techniques. We show from Figure 23 a clear increase in the amplitude of the relative time delays dt/t measured from ambient noise-based techniques, when modelling the impact of a local deformation in the reservoir in addition to the impact of the surface phenomena (blue circles in Figure 23). The impact of non-elastic processes, related for example to the creation of new fractures or the growth of pre-existing ones, is not quantified in our study. Such processes, which could be related at the laboratory scale to the development of damage, are expected to strongly modify the scattering properties of the medium, locally. An impact on the waveform coherence is expected to be highlighted following such medium perturbation.

The results of our numerical modelling open perspectives for the application of ambient noise-based monitoring techniques to the monitoring of deep geothermal reservoirs in various geotechnical contexts. The fine-scale evolution of the reservoir could be retrieved in quasi-real time from the application of such methods to the ambient noise records.

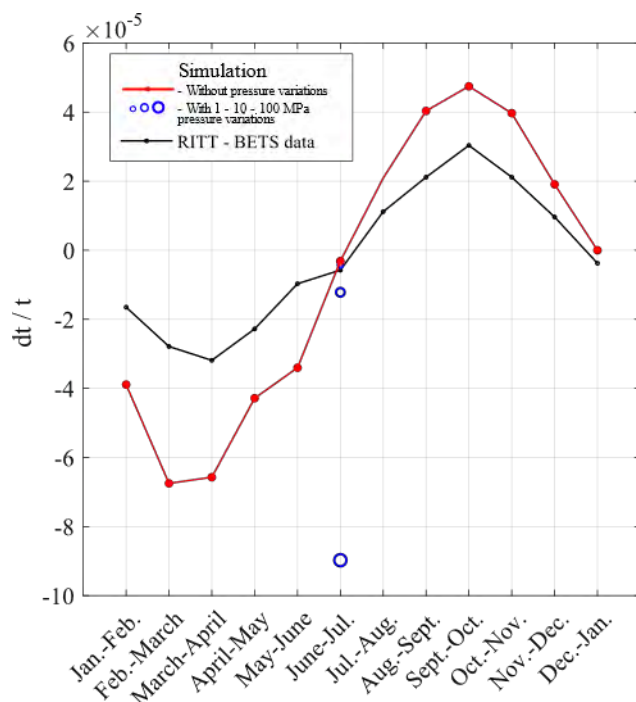


Figure 26 Annual variation of the optimum stretching coefficient measured in the simulation, by modelling the influence of the water table elevation and of surface temperature variations on the measurements (red dotted line). The interferometry measurements obtained when adding in the numerical model the contribution of a local perturbation in a kilometric asperity during the month of June are represented as blue circles. We consider pressure variations of 1, 10 and 100 MPa. The optimal stretching coefficient dt/t is measured by comparing the causal of the cross-functions. The 29 distinct measurements obtained for each pair of station separated by 2.6 km are averaged. The measurements are compared to the time series of the optimum stretching coefficient for the North components of RITT and BETS (black).

4.5 Conclusions and recommendations

We introduced CWI, and in particular, ANI, as a highly sensitive monitoring technique that has few requirements, but suffers from problems with the interpretation of the signals. Our results might provide new outcomes for their interpretation and for the application of the technique to monitor deep geothermal reservoirs.

Our research activities aimed to improve our understanding of the CWI measurements by questioning the relative contribution of different physical phenomena in the measurements, with a specific focus on the processes involved during the elastic deformation of a sample at the laboratory scale. From the modelling of effects highlighted in the laboratory experiments, we show that CWI measurements are stress sensitive and carry a real deformation signal. The identification of such deformation signals in the CWI measurements provides new possibilities for the use of interferometry technique based on ambient noise in order to monitor stress changes.

At the laboratory scale, we investigated the signature in the measurements of the mechanical loading of the sample within the elastic regime. We quantify the relative contribution of different phenomena involved in the elastic deformation of the sample, i.e., changes in the sample's shape and in its wave velocities, due either to density variations or acousto elastic effects. We highlight the preponderant influence of acousto-elastic effects related to non-linear elasticity. In addition, we measured the relative contribution of different phenomena involved during the thermo-elastic deformation of a Westerly granite sample.

Finally, we considered these results within a wider scale to study the applicability of ANI-based techniques to support reservoir management within various operational contexts such as hydraulic stimulations and in particular for the anticipation of unexpected changes. We propose a numerical model that aims first at identifying the surface processes at the origin of the temporal variations measured using the ambient noise recorded in the vicinity of Soultz-sous-Forêts and Rittershoffen deep geothermal projects. The identification of the processes at the origin of the measurements offers additional perspectives for the removal of unwanted effects in the monitoring of the reservoir evolution. We show that an unexpected change in the deep geothermal reservoir, modelled as a local pressurization applied at depth, could be monitored using ANI-based passive techniques.

Our measurements show that changes in relative time delays could be interpreted in the field by slight changes in the stress state in a reservoir rock mass. The loss of coherence between the waveforms could be interpreted by a local development of damage related to the growth or creation of new fractures. We introduced CWI, and in particular, ANI, as an interesting monitoring technique, which still suffers from problems associated with the interpretation of the measured signals. The research activities presented in this document might provide new outcomes for the application of the technique by contributing to the understanding of the CWI measurements.

By using continuously recording seismic networks, generally densely deployed around geothermal plants, the resolution and strong sensitivity of the CWI measurements could support reservoir management within various operational contexts. It could for example, contribute to the anticipation of unexpected changes such as transient aseismic deformations which could occur during the reservoir development. Such interferometry techniques could enable us to control the changes occurring in the stress state of the surrounding medium at depths or provide important observables, complementary to results obtained with standard micro-seismicity tools.

The development of such monitoring methods requires a more extensive use of the ambient seismic noise acquired in the vicinity of geothermal plants and the increase in the number of observables. For a given study site, it implies the establishment of dense seismic networks whose purpose is to improve the reliability of the monitoring by increasing the redundancy of the observations. The optimization of the geometry of the network requires, however, a more precise typological study, which depends on the location and specifics of the targeted site.

The application of these innovative methods implies also an improvement in the industrialization of the processing of noise records. Numerical methods have already been developed to automatize the treatment of ambient seismic noise records (Lecocq et al., 2014). However, further efforts would be necessary to apply them to the monitoring of geothermal reservoirs in operation, especially since the studies presented in this document show that the interpretation of the changes in terms of associated physical process is not trivial.

5 Bibliography

- Azzola, J., Griffiths, L., Schmittbuhl, J., Zigone, D., Magnenet, V., Masson, F., Heap, M. and Baud, P.: Coda wave interferometry during the heating of deep geothermal reservoir rocks, *Geothermal Energy*, 6(1), doi:10.1186/s40517-018-0107-2, 2018a.
- Azzola, J., Schmittbuhl, J., Zigone, D., Magnenet, V. and Masson, F.: Direct Modeling of the Mechanical Strain Influence on Coda Wave Interferometry, *Journal of Geophysical Research: Solid Earth*, 123(4), 3160–3177, doi:10.1002/2017JB015162, 2018b.
- Azzola, J., Valley, B., Schmittbuhl, J. and Genter, A.: Stress Characterization and Temporal Evolution of Borehole Failure at the Rittershoffen Geothermal Project, *Solid Earth Discussions*, 1–64, doi:10.5194/se-2019-72, 2019.
- Baujard, C., Genter, A., Cuenot, N., Mouchot, J., Maurer, V., Hehn, R., Ravier, G., Seibel, O., Vidal, J.: Experience from a successful soft stimulation and operational feedback after 2 years of geothermal power and heat production in Rittershoffen and Soultz-sous-Forêts plants (Alsace, France), *Geothermal Resources Council Transactions*, 2241-2252, 2018.
- Baujard, C., Genter, A., Dalmais, E., Maurer, V., Hehn, R., Rosillette, R., Vidal, J. and Schmittbuhl, J.: Hydrothermal characterization of wells GRT-1 and GRT-2 in Rittershoffen, France: Implications on the understanding of natural flow systems in the Rhine Graben, *Geothermics*, 65, 255–268, doi:10.1016/j.geothermics.2016.11.001, 2017.
- Bothara, J. K., Dhakal, R. P., Mander, J. B.: Seismic performance of an unreinforced masonry building: An experimental Investigation. *Earthquake Engineering and Structural Dynamics*, 39:45-68, 2010.
- Boxberger, T., Fleming, K., Pittore, M., Parolai, S., Pilz, M. and Mikulla, S.: The Multi-Parameter Wireless Sensing System (MPWise): Its description and application to earthquake risk mitigation, *Sensors*, 17, 2400, doi: 10.3390/s17102400, 2017.
- Brenguier, F., Campillo, M., Hadziioannou, C., Shapiro, N. M., Nadeau, R. M. and Larose, E.: Postseismic Relaxation Along the San Andreas Fault at Parkfield from Continuous Seismological Observations, *Science*, 321(5895), 1478–1481, doi:10.1126/science.1160943, 2008.
- Brenguier, F., Clarke, D., Aoki, Y., Shapiro, N. M., Campillo, M. and Ferrazzini, V.: Monitoring volcanoes using seismic noise correlations, *Comptes Rendus Geoscience*, 343(8–9), 633–638, doi:10.1016/j.crte.2010.12.010, 2011.
- Campillo, M. and Roux, P.: Crust and Lithospheric Structure - Seismic Imaging and Monitoring with Ambient Noise Correlations, in *Treatise on Geophysics*, pp. 391–417, Elsevier., 2015.
- Cees J.L. Willems, C. J.L., Ejderyan, O., Westaway, R., Burnside, N.M.: Public perception of geothermal energy at the local level in the UK, *World Geothermal Congress 2020, WGC 2020, April 26 – May 02 2020, Reykjavik, Iceland, 2020.*
- Chavot, P., Masseran, A., Bodin, C., Serrano, Y., Zoungrana, J.: Geothermal energy in France. A resource fairly accepted for heating but controversial for high-energy power plants. In: A. Pellizzone, A. Manzella, A. Allansdottir (eds.) *Geothermal Energy and Society*. Springer, *Lecture Notes in Energy*, 105-122. doi:10.1007/978-3-319-78286-7, 2019.
- Chavot, Ph., Heimlich, C., Masseran, A., Serrano, Y., Zoungrana, J., Bodin, C.: Social shaping of deep geothermal projects in Alsace: politics, stakeholder attitudes and local democracy. *Geothermal Energy*, 2018, 6 (26), <10.1186/s40517-018-0111-6, 2018.
- Cuenot, N., Genter, A.: Microseismic activity induced during recent circulation tests at the Soultz-sous-Forêts EGS power plant. *Proceedings World Geothermal Congress 2015, Melbourne, Australia, 19-25 April 2015.*
- Dorbath, L., Cuenot, N., Genter, A., Frogneux, M.: Seismic response of the fractured and faulted granite to massive water injection at 5 km depth at Soultz-sous-Forêts (France), *Geophysical Journal International*, 2009.

- Duputel, Z., Ferrazzini, V., Brenguier, F., Shapiro, N., Campillo, M. and Nercessian, A.: Real time monitoring of relative velocity changes using ambient seismic noise at the Piton de la Fournaise volcano (La Réunion) from January 2006 to June 2007, *Journal of Volcanology and Geothermal Research*, 184(1–2), 164–173, doi:10.1016/j.jvolgeores.2008.11.024, 2009.
- Ejderyan, O., Ruef, F., Stauffacher, M.: Geothermal Energy in Switzerland: Highlighting the role of context. In: A. Pellizzone, A. Manzella, A. Allansdottir (eds.) *Geothermal Energy and Society*. Springer, Lecture Notes in Energy, 239–257. doi:10.1007/978-3-319-78286-7, 2019.
- Filippou, F.C., Constantinides, M.: FEDEAS Lab – Getting Started Guide and Simulation Examples, NEEsgrid Report 2004-22 and SEMM Report 2004-05.
- Genter, A., Baujard, C., Cuenot, N., Hehn, R., Maurer, V., Mouchot, J., Seibel, O., Vidal, J.: Exploiting Fractured Granites for Producing Heat or Electricity - Dream or Reality?, 80th EAGE Conference and Exhibition 2018, Copenhagen, June 2018, Proceedings, EAGE Publications BVNetherlands, 2018.
- Griffiths, L., Lengliné, O., Heap, M. J., Baud, P. and Schmittbuhl, J.: Thermal Cracking in Westerly Granite Monitored Using Direct Wave Velocity, Coda Wave Interferometry, and Acoustic Emissions, *Journal of Geophysical Research: Solid Earth*, 123(3), 2246–2261, doi:10.1002/2017JB015191, 2018.
- Grigoli, F., Cesca, S., Priolo, E., Rinaldi, A. P., Clinton, J. F., Stabile, T. A., Dost, B., Garcia Fernandez, M., Wiemer, S., Dahm T.: Current challenges in monitoring, discrimination and management of induced seismicity related to underground industrial activities: a European perspective, *Review of Geophysics*, American Geophysical Union (AGU), DOI:10.1002/2016RG000542, 2017.
- Grigoli, F., Scarabello, L., Böse, M., Weber, B., Wiemer, S., Clinton, J.F.: Pick-and waveform-based techniques for real-time detection of induced seismicity. *Geophysical Journal International*, doi:10.1093/gji/ggy019, 2018.
- Grünthal, G., and European Seismological Commission: *European macroseismic scale 1998 : EMS-98 [2nd ed.]*. Luxembourg: European Seismological Commission Subcommission on Engineering Seismology Working Group Macroseismic scales, 1998.
- Haas, M., Wieland, M., Pittore, M.: DEMO: Remote Rapid Visual Screening (RRVS). Available online at: <http://vimeo.com/158600573>, 2016.
- Hillers, G., Husen, S., Obermann, A., Planès, T., Larose, E. and Campillo, M.: Noise-based monitoring and imaging of aseismic transient deformation induced by the 2006 Basel reservoir stimulation, *GEOPHYSICS*, 80(4), KS51–KS68, doi:10.1190/geo2014-0455.1, 2015.
- Hooijkaas, G. R., Genter, A. and Dezayes, C.: Deep-seated geology of the granite intrusions at the Soultz EGS site based on data from 5km-deep boreholes, *Geothermics*, 35(5–6), 484–506, doi:10.1016/j.geothermics.2006.03.003, 2006.
- Huenges, E., Ellis, J., Welter, S., Westaway, R., Min, K.B., Genter, A., Brehme, M., Hofmann, H., Meier, P., Wassing B., Marti M.: Demonstration of soft stimulation treatments in geothermal reservoirs, *World Geothermal Congress 2020, WGC 2020*, April 26 - May 02 2020, Reykjavik, Iceland, 2020.
- Hughes, D. S. and Kelly, J. L.: Second-Order Elastic Deformation of Solids, *Physical Review*, 92(5), 1145–1149, doi:10.1103/PhysRev.92.1145, 1953.
- Komatitsch, D. and Vilotte, J.-P.: The spectral element method: An efficient tool to simulate the seismic response of 2D and 3D geological structures, *Bulletin of the seismological society of America*, 88(2), 368–392, 1998.
- Kouris, L.A.S., Kappos, A.J.: A practice-oriented model for pushover analysis of a class of timber-framed masonry buildings, *Engineering Structures Journal*, Elsevier, 75: 489–506, 2014.
- Larose, E., Planes, T., Rossetto, V. and Margerin, L.: Locating a small change in a multiple scattering environment, *Applied Physics Letters*, 96(20), 204101, doi:10.1063/1.3431269, 2010.

- Lecocq, T., Caudron, C. and Brenguier, F.: MSNoise, a Python Package for Monitoring Seismic Velocity Changes Using Ambient Seismic Noise, *Seismological Research Letters*, 85(3), 715–726, doi:10.1785/0220130073, 2014.
- Lehuteur, M., Vergne, J., Schmittbuhl, J. and Maggi, A.: Investigating a deep geothermal reservoir using ambient noise correlation, in *EGU General Assembly Conference Abstracts*, vol. 16, p. 13798., 2014.
- Lehuteur, M.: Étude d'un réservoir géothermique profond par corrélation de bruit sismique ambiant, PhD Thesis, Université de Strasbourg, France, 2015.
- Lockner, D. A., Walsh, J. B. and Byerlee, J. D.: Changes in seismic velocity and attenuation during deformation of granite, *Journal of Geophysical Research*, 82(33), 5374–5378, doi:10.1029/JB082i033p05374, 1977.
- Mainsant, G., Larose, E., Brönnimann, C., Jongmans, D., Michoud, C. and Jaboyedoff, M.: Ambient seismic noise monitoring of a clay landslide: Toward failure prediction: seismic noise monitoring of a landslide, *Journal of Geophysical Research: Earth Surface*, 117(F1), n/a-n/a, doi:10.1029/2011JF002159, 2012.
- Megalooikonomou, K., Parolai, S., Pittore, M. 2018. Towards performance-driven risk monitoring and early warning system for geothermal platforms. *Geothermal Energy Journal*, Special Issue on Induced Seismicity <https://doi.org/10.1186/s40517-018-0094-3>.
- Megalooikonomou, K., Parolai, S., Pittore, M., 2018. Towards performance-driven seismic risk monitoring of geothermal platforms: development of ad hoc fragility curves, *Geothermal Energy*, 6:8, doi: 10.1186/s40517-018-0094-3.
- Michaels, J. E.: Detection, localization and characterization of damage in plates with an in situ array of spatially distributed ultrasonic sensors, *Smart Materials and Structures*, 17(3), 035035, 2008.
- Mignan, A., Karvounis, D., Broccardo, M., Wiemer, S., Giardini, D.: Including seismic risk mitigation measures into the Levelized Cost Of Electricity in enhanced geothermal systems for optimal siting. *Applied Energy*, 238, 831-850. <https://doi.org/10.1016/j.apenergy.2019.01.109>
- Murnaghan, F. D.: *Finite deformation of an elastic solid*, John Wiley & Sons., 1951.
- Obermann, A., Kraft, T., Larose, E. and Wiemer, S.: Potential of ambient seismic noise techniques to monitor the St. Gallen geothermal site (Switzerland), *Journal of Geophysical Research: Solid Earth*, 120(6), 4301–4316, doi:10.1002/2014JB011817, 2015.
- Peterschmitt, A., Hehn, R., Bosia, C., Cuenot, N., Pratiwi, A.S., Genter, A.: Risk assessment for chemical stimulation of EGS reservoirs: Application to EGS geothermal project In The Upper Rhine Graben, *Geothermal Resource Council Transactions*, 14-17th October, Reno, Nevada, USA, 2018.
- Pittore, M., Haas, M., Megalooikonomou, K.: Risk-orientated, bottom-up modeling of building portfolios with faceted taxonomies, *Frontiers in Built Environment*, 4:41, doi: 10.3389/fbuil.2018.00041, 2018.
- Planès, T. and Larose, E.: A review of ultrasonic Coda Wave Interferometry in concrete, *Cement and Concrete Research*, 53, 248–255, doi:10.1016/j.cemconres.2013.07.009, 2013.
- Poupinet, G., Ellsworth, W. L. and Frechet, J.: Monitoring velocity variations in the crust using earthquake doublets: An application to the Calaveras Fault, California, *Journal of Geophysical Research: Solid Earth*, 89(B7), 5719–5731, doi:10.1029/JB089iB07p05719, 1984.
- Rossetto, V., Margerin, L., Planès, T. and Larose, É.: Locating a weak change using diffuse waves: Theoretical approach and inversion procedure, *Journal of Applied Physics*, 109(3), 034903, doi:10.1063/1.3544503, 2011.
- Roux, P., Sabra, K. G., Gerstoft, P., Kuperman, W. A. and Fehler, M. C.: P-waves from cross-correlation of seismic noise: P waves from noise cross-correlations, *Geophysical Research Letters*, 32(19), n/a-n/a, doi:10.1029/2005GL023803, 2005.
- Shapiro, N. M. and Campillo, M.: Emergence of broadband Rayleigh waves from correlations of the ambient seismic noise: Correlation of Seismic noise, *Geophysical Research Letters*, 31(7), n/a-n/a, doi:10.1029/2004GL019491, 2004.

- Snieder, R.: Coda Wave Interferometry for Estimating Nonlinear Behavior in Seismic Velocity, *Science*, 295(5563), 2253–2255, doi:10.1126/science.1070015, 2002.
- Snieder, R.: The Theory of Coda Wave Interferometry, *Pure and Applied Geophysics*, 163(2–3), 455–473, doi:10.1007/s00024-005-0026-6, 2006.
- Vamvatsikos, D., Pantazopoulou, S.J.: Development of a simplified mechanical model to estimate the seismic vulnerability of heritage unreinforced masonry buildings. *Journal of Earthquake Engineering*, 20(2): 298-325, 2015.
- Yamamura, K., Sano, O., Utada, H., Takei, Y., Nakao, S., Fukao, Y.: Long-term observation of in situ seismic velocity and attenuation: In situ seismic velocity and attenuation measurement, *Journal of Geophysical Research: Solid Earth*, 108(B6), doi:10.1029/2002JB002005, 2003.

List of Figures

- Figure 1 Series of pictures taken during the acquisition campaign. A set of 11 buildings was selected for field measurements in Alsace around the geothermal sites to measure the fundamental period of these structures by analysing the ambient noise measured using the MPwise sensors. 5
- Figure 2 Visit of the Rittershoffen geothermal plant to thank local people that accepted the installation of the sensors in their homes. 6
- Figure 3 A prototype MP-Wise sensor installed on May the 14th 2018 in the town hall of the village of Keffenach. The sensor was customized by considering the specific fragility model of the building. 7
- Figure 4 Graphical User Interface (GUI) of the RRVS web-based platform. The bottom side includes multiple tabs for the manual entry of the observed structural features. The upper left panel shows an example of an omnidirectional image of a building located in the Soultz-sous-Forêts village, while in the upper right panel the same building (in green the related footprint) is shown in a GIS map (Pittore et al., 2018). 8
- Figure 5 The exposure model developed for the town and district of Soultz-sous-Forêts (from Megalooikonomou et al., 2018). The various classifications are as follows: MUR = Unreinforced Masonry, MR = Reinforced Masonry, RC = Reinforced Concrete, W = Wood, OTH = Other, 1= One floor - building, 2 = Two floors - building with rigid diaphragm, 3 = Two floors -building with flexible diaphragm..... 9
- Figure 6 Proposed analytical fragility curves for first damage state (pre-yielding damage state –DS1-0.1% drift limit for non-structural damage) for URM and TFM buildings for the cases of structures near the geothermal platforms near Soultz-sous-Forêts, France (Megalooikonomou et al., 2018) 11
- Figure 7 Result of the use of two different fuzzy mapping schemes applied to the building inventory collected in Soultz-sous-Forêts. The resulting exposure models are therefore based on the same information, but refer to two vulnerability schemas. The DESTRESS exposure/vulnerability model has been developed within the project considering the specific features of the residential buildings observed in-situ. The EMS-98 schema is a well-known classification proposed as part of the European Macroseismic Scale (EMS-98, Grünthal et al., 1988) and is largely used in risk applications, especially for unreinforced masonry buildings. 11
- Figure 8 Principle behind the numerical experiment. We impose a mechanical loading to a numerical sample imposing a rigid step-by-step displacement δ to its upper face. During the loading, a Ricker wavelet (see left insert) is sent in the medium from the source and recorded at the opposite face by the receiver (see right insert). The waveforms are recorded for 32 positions of the receiver equally distributed along the right-hand boundary of the sample. 15
- Figure 9 Image of the experimental apparatus. The piston of a servo controlled 10 T press loads a holed block of Au4G (70 holes of radius 3 mm). Two linear acoustic arrays of 32 sensors are held in direct contact with the boundaries of the sample. At each step of the displacement imposed by the piston, the element of the transducer on the left which is located at the middle of the array sends a pulse wave. This wave is recorded by each of the 32 elements transducer located on the opposite face of the sample. An image correlation technique is used to estimate the displacement field by comparing pictures of the sample taken at each step of the loading procedure. 16
- Figure 10 a) The logarithmic and normalized expression of the energy density, $\ln U(t)$, is computed with measurements obtained in the laboratory (plain black curve) and in the simulation (plain red curve), in an unstressed medium. The 32 functions computed from records obtained at each sensor of the receiver line are averaged spatially. The best fits to the laboratory and numerical measurements, determined by the least square's regression to estimate the mean free path, are plotted as dashed curves (respectively dashed black and dashed red lines). b) experimental displacement field $u_Y(X, Y)$ calculated from image correlation between a picture of the unstressed sample and one captured after imposing a displacement of $\delta = 60 \mu\text{m}$ to the top of the sample (corresponding to an applied force of $F = 75 \text{ kN}$). c) Numerical displacement field $u_Y(X, Y)$ computed by Code_Aster when applying the same loading and using the same color scale. The holes introduced in the sample are represented by black circles with the same size and spatial locations. The red bar indicates the extent of contact zone between the sample and the piston. . 17
- Figure 11 Coda wave interferometry. a) Comparison of three synthetic waveforms recorded respectively for an imposed displacement $\delta = 0 \mu\text{m}$ (black), $\delta = 75 \mu\text{m}$ (blue), and $\delta = 150 \mu\text{m}$ (red); b) zoom in a $6.5 \mu\text{s}$ window of the waveform at the beginning of the coda where a negligible time shift is observed and c) zoom at the end of the waveform where the time shift is clearly sensitive to the imposed displacement. d) Time shifts within the coda measured with either a time window correlation technique (circles) or a frequency stretching technique (solid line) when comparing waveforms at 75 and 0 μm displacement

- (blue) and at 150 and 0 μm displacement (red). The lines fitted on the time shifts measured by a time window correlation technique (circles) allows the relative time shift dt/t to be measured. 18
- Figure 12 Comparison between the linear regression fitted to the time shifts dt/t of the laboratory experiments (black line) and the ones obtained from simulations based on three distinctive models as a function of the stress σ_Y . The red dotted line (model 1) depicts the measurements when modelling all the influences on dt/t of: the change in the sample shape, the change in the wave velocity variations due to density variations, and those due to acousto-elastic effects using the third-order elastic coefficient (TOEC) of aluminum. Model 2 corresponds to the relative contribution of the change of sample shape including the boundaries of the holes (i.e., the scatters) (red plain line). Model 3 is an extended version of Model 2 with also the wave velocity variations due to density variations (red dashed line). Relative time shifts are the mean values calculated from the 32 distinctive estimates obtained along the receiver array. 19
- Figure 13 a) Sketch of the experimental setup (modified from Griffiths et al. 2018) for wave velocity measurements on a Westerly Granite sample. The apparatus consists of a uniaxial press, a tube furnace and for waveform measurements, a pair of high temperature resistant and broadband acoustic sensors that are set in direct contact with opposing ends of the sample [see Griffiths et al. (2018) for details]. Upper acoustic sensor is the source and the lower one is the receiver. b) Evolution with time during three heating/cooling cycles, of the temperature measured at the center of the sample with a thermocouple inserted into a hole drilled radially. 20
- Figure 14 The logarithmic and normalized expression of the energy density $\ln U(t)$, represented both in the experimental case (red line) and in the simulated case (blue line), characterizes the scattering properties and is used for the linear inversion of the mean free path. The comparison of both functions shows that the numerical medium reproduces the wave scattering happening in the experimental sample. The dashed black line corresponds to the best fit to the laboratory measurements using the diffusion model and leading to an estimate of the mean free path $l = 3.9 \text{ mm}$ 21
- Figure 15 Comparison of simulated and laboratory CWI measurements. We represent the CWI measurements obtained in the laboratory (orange line) during the second heating cycle of Westerly Granite and in the simulation (blue line) with temperature measured at the middle of the sample. Relative time delays are measured by comparing the waveform recorded at a given temperature with respect to the “reference” waveform. A linear regression is fitted to the measurements to estimate the slopes -0.13×10^{-4} to numerical results and -1.62×10^{-4} to laboratory measurements (blue line and red line, respectively). 22
- Figure 16 Comparison of laboratory CWI measurements during the first cycle (red line) with the simulated CWI measurements obtained without (blue line) and with (black line) introduction of a dependency with temperature of the bulk modulus K and of the Young’s modulus E . A linear regression is fitted to the measurements. The slope of the linear regression fitted to the simulated CWI results is -0.13×10^{-4} without introduction of the temperature dependency and it is -4.1×10^{-4} when the dependency is added to the simulation. 22
- Figure 17 Delays (red) and decoherence (black) with time in the signal, measured in simulations during the elastic deformation of the sample due to a $75 \mu\text{m}$ displacement of the upper face of the sample. The measurement, obtained in overlapping windows $6.5 \mu\text{s}$, is obtained at middle sensor of the receiver line (left) or is spatially averaged over the 32 sensors of the receiver line (right). 23
- Figure 18 normalized values of temporally averaged decoherence and delays (respectively black and red; measurements in successive windows in the signal are averaged at each sensor of the receiver line) with position along the right boundary. The measurements obtained in the simulation (plain line) and in the laboratory experiments (dashed line) are compared to the volumetric strain, averaged horizontally and measured using Code_Aster, to investigate the spatial variability and the sensibilities of both measurements. 24
- Figure 19 Principle of the experiments where a $75 \mu\text{m}$ displacement is applied to the boundary of one of the 70 round scatterers in two different ways. a) The perturbed medium is obtained by shifting the position of the round scatterer by $75 \mu\text{m}$ in the mesh grid before it is discretized again. b) The perturbed medium is obtained by deforming the mesh grid using Code_Aster. The homogeneous displacement of $75 \mu\text{m}$ is a boundary condition in the mechanical problem. 25
- Figure 20 The spatial variability of delays (left) and decoherence (right), averaged temporally in the signal length and normalized, are measured with the position of the sensor along the receiver line (blue dotted line). The displacement (black line, right) and the volumetric strain (black line, left) are measured within

the sample by Code_Aster, the latter being estimated from the trace of the strain tensor. The measurements are averaged horizontally..... 26

Figure 21 The spatial variability of decoherence, averaged temporally in the signal length and normalized, are measured with the position of the sensor along the receiver line (blue dotted line). The norm of the displacement (black line) is measured within the sample and averaged horizontally..... 27

Figure 22 Overview of the localization of the Rittershoffen and Soultz-sous-Forêts EGS projects, in the upper Rhine Graben, as well as an overview of the RT seismic network deployed in the vicinity Bottom: data availability over time for the RT network. The grey periods noted “GRT1” and “GRT2” correspond to the drilling periods of the wells at the Rittershoffen site and “STIM” corresponds to the stimulation of the GRT1 well..... 28

Figure 23 a): time series of the optimum stretching coefficient for the North components of RITT and BETS, filtered between 1 and 3 Hz, and stacked monthly for the period from 2012 to 2017. b) and c): Annual surface temperature (lefts) and water table elevation converted into pressure (right) presented in absolute values (line) or in terms of monthly variations (bars). The mean surface temperature is measured monthly in Rittershoffen. The water table elevation is measured weekly at the nearby Haguenuau hydrological station. The measurements are stacked monthly for the period from 2012 to 2017 and converted into pressure. 29

Figure 24 Principle of the numerical model developed to model the signature on the interferometry measurements of annual surface temperature and water table elevation variations and local changes within the reservoir. The sample consists in a 2D representation of a geological section down to 22.4km under Rittershoffen, in which the boundary conditions for the deformation modelling (i.e., surface temperature and pressure variations) act superficially and the deep part with large heterogeneities aim at scattering the wavefield propagated from the source in the seismic propagation modelling. 30

Figure 25 The scattering properties are characterized from the measurement of the temporal variation of the seismic energy using the cross-functions of the north components of the RITT and BETS stations (dashed line), and from the cross-functions measured in the simulation (plain line). We show a logarithmic and normalized expression of the energy density, measured with the causal (red) and acausal (blue) part of the cross-function, enabling to estimate by least square regression to a diffusion model, the mean free paths. Black line shows the best fit determined by the least square method. 31

Figure 26 Annual variation of the optimum stretching coefficient measured in the simulation, by modelling the influence of the water table elevation and of surface temperature variations on the measurements (red dotted line). The interferometry measurements obtained when adding in the numerical model the contribution of a local perturbation in a kilometeric asperity during the month of June are represented as blue circles. We consider pressure variations of 1, 10 and 100 MPa. The optimal stretching coefficient dt/t is measured by comparing the causal of the cross-functions. The 29 distinct measurements obtained for each pair of station separated by 2.6 km are averaged. The measurements are compared to the time series of the optimum stretching coefficient for the North components of RITT and BETS (black). 32

Imprint

Project Lead	GFZ German Research Centre for Geosciences Telegrafenberg 14473 Potsdam (Germany) www.gfz-potsdam.de/en/home/
Project Coordinator	Prof. Ernst Huenges huenges@gfz-potsdam.de +49 (0)331/288-1440
Project Manager	Dr. Justyna Ellis ellis@gfz-potsdam.de +49 (0)331/288-1526
Project Website	www.destress-h2020.ch
Report Authorship	Azzola J., Schmittbuhl J., Zigone D., Lengliné O., Magnenet V., Masson F., Fleming K., Pittore M., Megalooikonomou K. G., Maurer V., Richard A., Genter A. (2019). Non-standard risk monitoring, Destress report, Deliverable D3.4, August 2019, 41 pp.
Copyright	Copyright © 2019, DESTRESS consortium, all rights reserved

Liability claim

The European Union and its Innovation and Networks Executive Agency (INEA) are not responsible for any use that may be made of the information any communication activity contains.

The content of this publication does not reflect the official opinion of the European Union. Responsibility for the information and views expressed in the therein lies entirely with the author(s).

DESTRESS is co-funded by

National Research Foundation of Korea (NRF)
Korea Institute for Advancement of Technology (KIAT)
Swiss State Secretariat for Education, Research and Innovation (SERI)